IOP Publishing Phys. Biol. 23 (2026) 016002 https://doi.org/10.1088/1478-3975/ae2c34

Physical Biology

PAPER

The interaction between dynamic ligand signaling and epigenetics in Notch-induced cancer metastasis

Tianchi Chen[1], **M Ali Al-Radhawi**[2], **Herbert Levine**[3,*] and **Eduardo D Sontag**[2,*]

[1] Department of Bioengineering, Northeastern University, Boston, MA, United States of America
[2] Departments of Electrical and Computer Engineering and Bioengineering, Northeastern University, Boston, MA, United States of America
[3] Departments of Physics and Bioengineering, and Center for Theoretical Biological Physics, Northeastern University, Boston, MA, United States of America
[*] Authors to whom any correspondence should be addressed.

E-mail: h.levine@northeastern.edu and e.sontag@northeastern.edu

Keywords: metastasis, melanoma, Notch signaling, miR-222, epigenetics

Supplementary material for this article is available online

OPEN ACCESS

RECEIVED
19 May 2025

REVISED
20 November 2025

ACCEPTED FOR PUBLICATION
12 December 2025

PUBLISHED
30 December 2025

Abstract

Metastatic melanoma presents a formidable challenge in oncology due to its high invasiveness and resistance to current treatments. Central to its ability to metastasize is the Notch signaling pathway, which, when activated through direct cell–cell interactions, propels cells into a metastatic state through mechanisms akin to the epithelial-mesenchymal transition (EMT). While the upregulation of miR-222 has been identified as a critical step in this metastatic progression, the mechanism through which this upregulation persists in the absence of active Notch signaling remains unclear. Here we introduce a dynamical system model that integrates miR-222 gene regulation with histone feedback mechanisms. Through computational analysis spanning both sustained and pulsatile ligand inputs, we delineate the non-linear decision boundaries that govern melanoma cell fate transitions, taking into account the dynamics of Notch signaling and the role of epigenetic modifications. Dimensional analysis reduces the 11-parameter system to three critical control groups governing chromatin modification rates and feedback strengths, providing a theoretical framework for parameter selection in the absence of complete kinetic measurements. Global sensitivity analysis identifies PRC2-mediated methylation and KDM5A-mediated demethylation as the dominant control parameters, while stochastic simulations show population heterogeneity consistent with the variable EMT responses observed in cancer cell populations. Our analysis examines the interplay between Notch signaling pathways and epigenetic regulation in dictating melanoma cell fate.

1. Introduction

Cancer metastasis represents a primary cause of mortality, with the epithelial-mesenchymal transition (EMT) playing a key role in conferring metastatic capabilities upon cancer cells [1–3]. The EMT, characterized by its reversibility, is modulated by a diverse array of environmental cues, EMT-inducing transcription factors (EMT-TFs), and epigenetic regulators [4, 5]. This research specifically targets melanoma, notable for its high resistance to treatment and propensity for metastasis.

The Notch signaling pathway is a critical player in development and disease, including metastasis [6–8]. It regulates cellular differentiation, proliferation, and fate determination [9]. In melanoma, Notch activation, for instance by keratinocytes expressing Notch ligands, can promote metastasis, partly through inhibition of the lineage survival oncogene MITF [10]. Conventionally, Notch activation requires direct cell-to-cell contact. However, melanoma cells can maintain a metastatic phenotype even after losing contact with ligand-expressing cells, suggesting a mechanism for persistence or memory [10].

A powerful approach to describe and resolve the complex interactions and feedback loops involved in genetic and epigenetic regulation is dynamical system modeling [11–13]. In particular, such methods

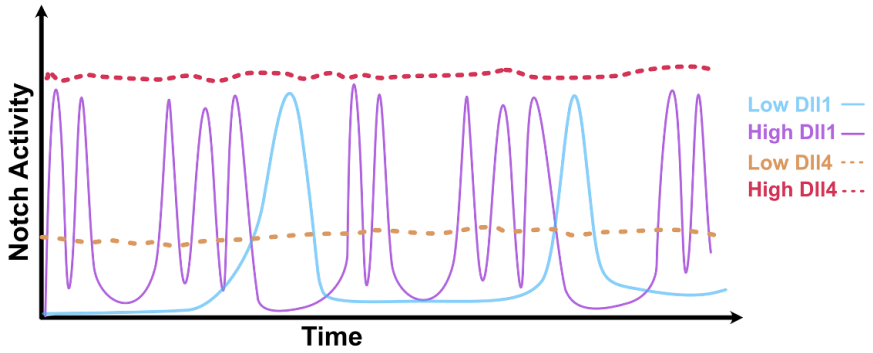

Figure 1. A conceptual view of distinct Notch signaling dynamics induced by DLL1-like and DLL4-like ligands. Experimental evidence suggests DLL1-like ligands can induce pulsatile NICD signals, In contrast, DLL4-like ligands tend to induce more sustained signals with an amplitude that increases with the concentration level of the ligand [20, 21]. The characteristics of these signals (amplitude, frequency, duration) can influence downstream cellular responses.

can be applied to regulatory mechanisms involving histone modifications such as H3K4me3 (activating) and H3K27me3 (repressive), which play an important role in EMT and cancer progression [14–16]. We propose that an epigenetic switching mechanism, involving feedback regulation of histone modifying enzymes, underlies the persistence of the Notch-induced metastatic state in melanoma. Specifically, we model the regulation of miR-222, whose expression is linked to melanoma metastasis [17] and influenced by Notch [10]. Our model incorporates the competition between NICD (the activated Notch intracellular domain) and MITF for the TF RBPJ, and links this competition to the recruitment of the H3K4me3 demethylase KDM5A [18], thereby influencing the histone state at the miR-222 locus. We hypothesize that positive feedback loops in the histone modification system create bistability, allowing the miR-222 locus to be switched to, and maintained in, an active state by a transient Notch signal. Computational analysis yields switching times within the experimentally observed EMT window [10, 19], with stochastic simulations (SI section 6) showing how intrinsic molecular noise generates population heterogeneity: the model predicts that only a fraction of cells undergo complete EMT under identical signaling conditions, reflecting the probabilistic nature of epigenetic state transitions.

Furthermore, different Notch ligands, such as DLL1-like and DLL4-like, can elicit distinct temporal dynamics of NICD activation—often pulsatile for DLL1-like and sustained for DLL4-like (figure 1) [20, 21]. These distinct dynamics can lead to differential activation of target genes [20]. A key question is how these dynamics are interpreted by downstream regulatory circuits. Our model investigates how the proposed epigenetic switch responds to both sustained (DLL4-like) and pulsatile (DLL1-like) NICD inputs, exploring whether the switch exhibits frequency-dependent filtering properties. We find that the epigenetic switch acts as a low-pass filter, which may place high-frequency DLL1-like signals at a relative disadvantage compared to sustained DLL4-like signals for initiating this specific epigenetic transition.

The manuscript is organized as follows. We introduce the computational model linking ligand-dependent NICD competition to miR-222 epigenetic regulation. We then analyze the model's bistable behavior and its response to sustained and pulsatile NICD signals, characterizing the switching boundaries (amplitude–frequency, A–ω, with A denoting signal amplitude and ω denoting signal frequency) and switching times (ST–ω, with ST denoting the switching time). We investigate how altering epigenetic parameters, particularly PRC2 feedback strength, reshapes these response characteristics. Finally, we discuss the implications of the model for dynamic signal processing, epigenetic memory, and therapeutic relevance. SI sections 2–6 provide the extended analyses, including the nondimensional formulation, sensitivity and Monte Carlo screens, waveform robustness tests, solver benchmarking, and stochastic pulse-counting simulations.

2. Methods

2.1. Model description

Our model (figure 2) integrates Notch signaling input with epigenetic regulation of miR-222. It consists of two coupled modules.

Module 1: NICD-MITF competition. Upon Notch receptor activation by a ligand, the notch intracellular domain (NICD, denoted N) is released and translocates to the nucleus, where it undergoes rapid turnover through proteasomal degradation on the timescale of hours [22, 23]. There, it competes with

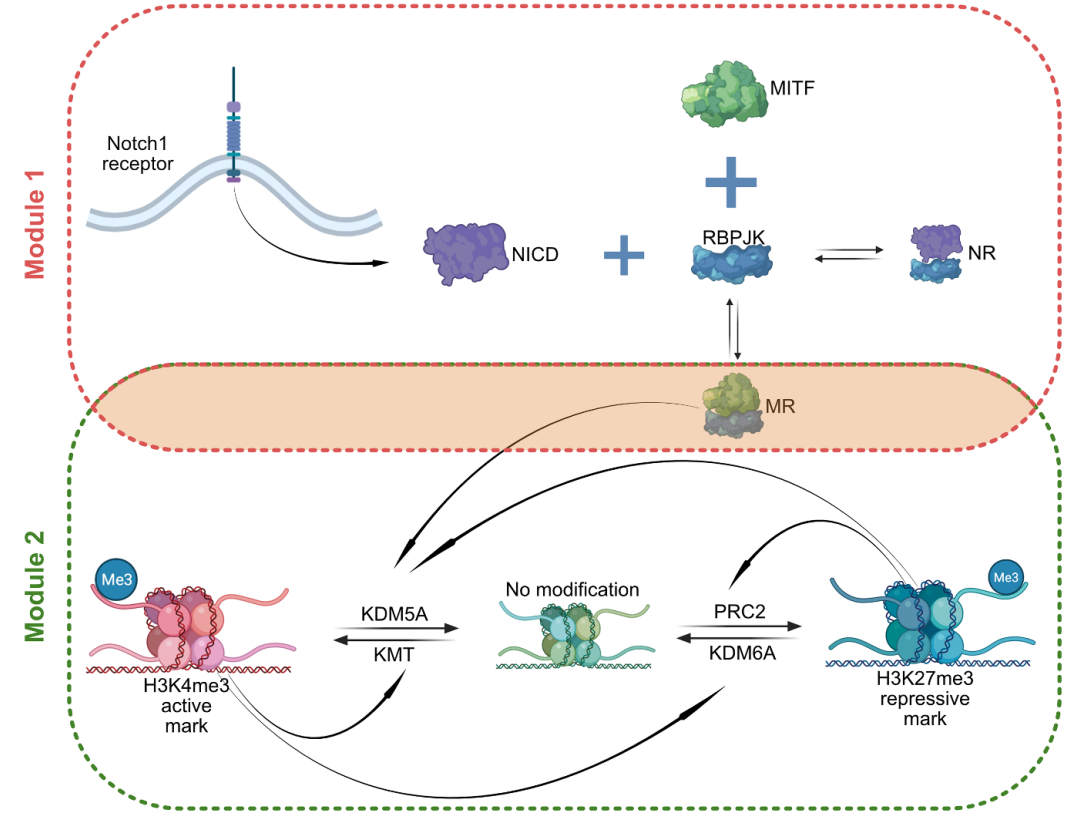

Figure 2. Schematic description of the Notch-EMT model with epigenetic regulations. The model comprises two modules. Module 1 (red dashed region): NICD (N) release is triggered by Notch activation. N competes with MITF (M) for binding to RBPJ (R). High N leads to formation of NR and reduces the level of the MR complex. Module 2 (green dashed region): Represents the epigenetic state of the miR-222 locus via three histone states: H4 (Active, H3K4me3), H27 (Repressive, H3K27me3), and H0 (Unmarked/Void). Transitions are mediated by histone modifying enzymes (KMT, KDM6A, PRC2, KDM5A). Positive feedback (H4 promotes KMT/KDM6A; H27 promotes PRC2/KDM5A) allows for bistability. Coupling: The MR complex enhances KDM5A activity, linking Notch signaling (via MR levels) to the epigenetic state.

the TF MITF (M) for binding to the DNA-binding protein RBPJ (R). In the absence of NICD, MITF binds RBPJ to form the MR complex. When NICD is present, it binds RBPJ to form the NR complex, thereby reducing the amount of available R and consequently reducing the concentration of the MR complex. The production rate of N, denoted 'Signal(t)', represents the strength and dynamics of the external Notch ligand stimulus.

Module 2: Epigenetic regulation of miR-222. We model the histone state associated with the miR-222 gene locus using three states: H4 (representing an active state, high H3K4me3), H27 (representing a repressed state, high H3K27me3), and H0. The H0 state represents an unmarked or intermediate chromatin configuration. In our model, this state is assumed to correspond to a basal or low level of miR-222 transcription, distinct from the actively repressed H27 state (low/off miR-222) and the highly active H4 state (high miR-222). It primarily serves as a transient state through which the locus passes during switching between the H4 and H27 states. The transitions between these states are governed by the activity of four types of histone modifying enzymes: KMTs (adding H3K4me3), KDM6A (removing H3K27me3), PRC2 (adding H3K27me3), and KDM5A (removing H3K4me3). Crucially, the model includes positive feedback loops: the H4 state promotes the production/activity of KMT and KDM6A, while the H27 state promotes the production/activity of PRC2 and KDM5A. This double-positive feedback structure can generate bistability between the H4-high and H27-high states.

Module coupling. The two modules are linked via the MR complex. Based on experimental findings [10, 18], we assume that the MR complex enhances the production or recruitment of the H3K4me3 demethylase KDM5A to the miR-222 locus. Therefore, high MITF activity (high MR, low NICD) promotes the H27 state (miR-222 repression), while high Notch activity (low MR, high NICD) disinhibits KDM5A recruitment, allowing the feedback loops to potentially switch the system to the H4 state (miR-222 activation).

Table 1. CRN model of the Notch-miR222 circuit. Module 1 is driven by input NICD (N) concentration (Signal(t)) and reflects the NICD competition with MITF (M) for RBPJ (R). Module 2 describes the epigenetic regulation of histone states (H4, H0, H27) via enzymes (KDM5A, KDM6A, PRC2, KMT), including feedback loops and basal production/degradation. The modules are coupled via MR-enhanced KDM5A production/recruitment (rate k_0).

NICD, MITF competition (R1-R2)	$R \underset{k_3}{\overset{\text{Signal}(t)}{\rightleftharpoons}} NR$ $M + R \underset{k_2}{\overset{k_1}{\rightleftharpoons}} MR$
Core histone regulation (Module 2)	$H4 + KDM5A \xrightarrow{d} H_0 + KDM5A$ $H0 + PRC2 \xrightarrow{m} H27 + PRC2$ $H27 + KDM6A \xrightarrow{d1} H0 + KDM6A$ $H0 + KMT \xrightarrow{m1} H4 + KMT$
Epigenetic feedback (Module 2)	$MR \xrightarrow{k_0} MR + KDM5A$ (MR induction of KDM5A) $H27 \xrightarrow{p} H27 + PRC2$ (H27 feedback on PRC2) $H4 \xrightarrow{kk} H4 + KDM6A$ (H4 feedback on KDM6A) $H4 \xrightarrow{pp} H4 + KMT$ (H4 feedback on KMT) $H27 \xrightarrow{k} H27 + KDM5A$ (H27 feedback on KDM5A)
Enzyme Production (Module 2)	$\varnothing \xrightarrow{\alpha_1} KDM6A$ $\varnothing \xrightarrow{\alpha_1} KMT$ $\varnothing \xrightarrow{\alpha_1} PRC2$ $\varnothing \xrightarrow{\alpha_1} KDM5A$ (Basal production)
Enzyme Degradation (Module 2)	$PRC2 \xrightarrow{\delta} \varnothing$ $KDM5A \xrightarrow{\delta} \varnothing$ $KDM6A \xrightarrow{\delta} \varnothing$ $KMT \xrightarrow{\delta} \varnothing$

Mathematical model

We formulated the model using chemical reaction networks (CRNs) [24], assuming mass-action kinetics (table 1).

State variables are the concentrations of the molecules listed in table 2.

Parameters. table 3 lists the parameter sets used throughout the manuscript. Set A underpins figures 3 and 4, whereas Set B represents the higher-feedback regime employed for the PRC2 modulation sweep in figure 5. These sets follow from the non-dimensional analysis and parameter sweeps detailed under 'Parameter Estimation Methodology' in section 2, ensuring bistable switching, realistic timescales, and experimentally motivated ligand responses. Unless otherwise noted, simulations adopt these values together with the ligand input definitions given later in section 2.

Modeling time-varying signals

To simplify our analysis, we model time-varying pulsatile signals by square waves. On the other hand, it has been observed experimentally that Notch signaling often exhibits exponential NICD decay with measured half-lives of 2–4 h following ligand binding [20, 22, 23]. Thus, in order to assess model robustness to waveform shape, we implemented exponential decay signals with time constants $\tau = 2$, 5, and 10 h and systematically explored the amplitude–frequency parameter space (SI section 4, figure S4). Exponential pulses require 4–8 fold higher amplitudes than square waves to achieve switching (e.g. $\tau = 2$ h pulses need $\geqslant$400 nM versus 50 nM for square waves at equivalent frequency). The non-monotonic frequency-amplitude boundary persists across waveforms, with efficient switching occurring when signal frequency matches chromatin timescales ($\omega \approx 1/\tau_c$). These results confirm frequency-dependent signal integration as an intrinsic property of chromatin feedback architecture. We retain square pulses in the main text for clarity while demonstrating waveform robustness in the SI.

Units and plotting conventions

Time is reported in hours, ω in h^{-1}, and kinetic rates in h^{-1} unless specified. Concentrations are normalized (a.u.) and consistent across figures. All axes include units in labels, and all figures use the Wong colorblind-safe palette [25] with consistent line styles for accessibility.

Table 2. State variables of the CRN model.

State Variable	Description
R	Free RBPJ concentration.
NR	RBPJ bound to NICD complex concentration.
M	Free MITF concentration.
MR	MITF-RBPJ complex concentration.
H4	Concentration of loci in the 'Active' histone state (high H3K4me3).
H0	Concentration of loci in the 'Unmarked/Void' histone state.
H27	Concentration of loci in the 'Repressive' histone state (high H3K27me3).
KDM5A	H3K4me3 demethylase concentration.
KDM6A	H3K27me3 demethylase concentration.
PRC2	H3K27me3 methyltransferase concentration.
KMT	H3K4me3 methyltransferase concentration.

Table 3. Parameters of the CRN model and default values used. Total amounts of M, R, and histone sites (H0+H4+H27) are conserved or implicitly set. Set A drives the sustained/pulsatile trajectories and A–ω sweeps; Set B underlies the PRC2 modulation sweep. Entries marked with [a] were varied in the Sobol global sensitivity analysis (SI section 3). The parameter values emerge from systematic dimensional analysis (SI section 2) that reduces the 11-parameter model to three control groups governing bistable switching: $\Pi_2 = d \cdot \tau_c \cdot E_c/H_c$ (H3K4me3 demethylation timescale), $\Pi_3 = m \cdot \tau_c \cdot E_c/H_c$ (H3K27me3 methylation timescale), and $\Pi_4 = pp/kk$ (feedback strength ratio). Set A yields $\Pi_2 \approx 1.0$, $\Pi_3 \approx 2.0$, $\Pi_4 = 6.0$, positioning the system on the mesenchymal-favoring side of the bistable manifold; Set B yields $\Pi_2 \approx 3.9$, $\Pi_3 \approx 2.0$, $\Pi_4 = 1.0$, representing a higher-demethylation, balanced-feedback regime for PRC2 modulation studies. Both sets were selected from 2252 validated bistable configurations (47% of 4800 tested combinations) to maintain EMT transition timescales on the order of hours to days, consistent with melanoma progression [10, 19]. The characteristic scales used are $\tau_c = 24$ h (representative day-scale EMT timescale) and $E_c/H_c = 0.2$ (typical enzyme-to-histone stoichiometry).

Parameter	Value (Set A: figures 3 and 4)	Value (Set B: figure 5)	Description
A	Varies	Varies	NICD signal amplitude
ω	Varies	Varies	NICD pulse frequency
ϕ	Varies	Varies	NICD pulse phase
k_3	1.0	1.0	NR dissociation rate (normalized)
k_1	1.0	1.0	M-R binding rate
k_2	1.0	1.0	MR unbinding rate
k_0	1.0	1.0	MR-driven KDM5A recruitment
d[a]	0.21	0.81	KDM5A-mediated H4 demethylation
d_1	1.0	1.0	KDM6A-mediated H27 demethylation
m[a]	0.41	0.41	PRC2-mediated H0 $\rightarrow$ H27 methylation
m_1	1.0	1.0	KMT-mediated H0 $\rightarrow$ H4 methylation
p	6.0	16.0	H27-enhanced PRC2 production
k	0.0	0.0	H27-enhanced KDM5A production
pp[a]	6.0	11.0	H4-enhanced KMT production
kk[a]	1.0	11.0	H4-enhanced KDM6A production
α_1	1.0	1.0	Basal enzyme production rate
δ	1.0	1.0	Enzyme degradation rate

[a] Parameters varied in the Sobol global sensitivity analysis (SI section 3).

Ordinary differential equations (ODEs)

The corresponding **ODEs** derived from table 1 assuming mass-action kinetics are:

$$\frac{\mathrm{d}[R]}{\mathrm{d}t} = -\mathrm{Signal}(t)\cdot[R] + k_3[NR] - k_1[M][R] + k_2[MR], \quad (1)$$

$$\frac{\mathrm{d}[NR]}{\mathrm{d}t} = \mathrm{Signal}(t)\cdot[R] - k_3[NR], \quad (2)$$

$$\frac{\mathrm{d}[M]}{\mathrm{d}t} = -k_1[M][R] + k_2[MR], \quad (3)$$

$$\frac{\mathrm{d}[MR]}{\mathrm{d}t} = k_1[M][R] - k_2[MR], \quad (4)$$

$$\frac{\mathrm{d}[KDM5A]}{\mathrm{d}t} = \alpha_1 + k_0[MR] + k[H27] - \delta[KDM5A], \quad (5)$$

$$\frac{\mathrm{d}[H4]}{\mathrm{d}t} = -d[H4][KDM5A] + m_1[H0][KMT], \quad (6)$$

$$\frac{\mathrm{d}[H0]}{\mathrm{d}t} = d[H4][KDM5A] - m[H0][PRC2] + d_1[H27][KDM6A] - m_1[H0][KMT], \quad (7)$$

$$\frac{\mathrm{d}[PRC2]}{\mathrm{d}t} = \alpha_1 + p[H27] - \delta[PRC2], \quad (8)$$

$$\frac{\mathrm{d}[H27]}{\mathrm{d}t} = m[H0][PRC2] - d_1[H27][KDM6A], \quad (9)$$

$$\frac{\mathrm{d}[KDM6A]}{\mathrm{d}t} = \alpha_1 + kk[H4] - \delta[KDM6A], \quad (10)$$

$$\frac{\mathrm{d}[KMT]}{\mathrm{d}t} = \alpha_1 + pp[H4] - \delta[KMT]. \quad (11)$$

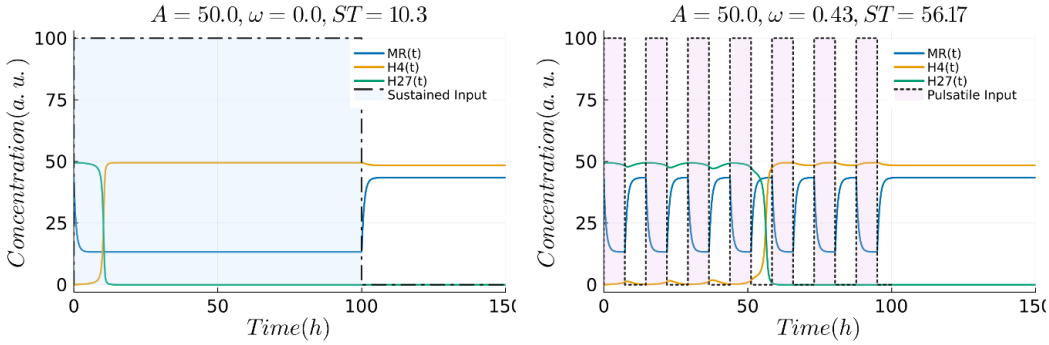

(a) Sustained DLL4-like signal (b) Pulsatile DLL1-like signal

Figure 3. Both sustained (DLL4-like) and pulsatile (DLL1-like) NICD dynamics can induce persistent switching of the miR-222-associated histone state. Simulations start from the H27-high state (blue). Signal is applied from $T = 0$ to $T = 100$ ($\Delta T = 100$). Panel (a) uses a sustained input ($Signal(t) = A = 50$) that triggers a switch to the H4-high state (red), which persists after signal removal; panel (b) shows a pulsatile input ($SLignal(t) = 50 \times [1 + \text{sign}(\cos(0.43\,t))]/2$, $\phi = 0$) that also drives persistent switching. Units: time (h), concentration (a.u.).

Conservation laws hold for total RBPJ ($R_{\text{tot}} = [R] + [NR] + [MR]$), total M ($M_{\text{tot}} = [M] + [MR]$), and all possible Histone modifications ($H_{\text{tot}} = [H0] + [H4] + [H27]$).

Region of bistability

A key goal of this model is to explain the observed persistence of the metastatic phenotype even after the initiating Notch signal is removed [10]. We hypothesize that this persistence arises from epigenetic memory, mechanistically represented in the model by bistability within the epigenetic module (Module 2). This bistability allows the system to switch between two stable steady states—one corresponding to low miR-222 expression (i.e. H27-high) and another to high miR-222 expression (H4-high)—and remain in the new state after a transient input.

The existence of bistability is fundamental to the model's ability to exhibit epigenetic memory. We employed standard numerical methods for finding steady states and performing linear stability analysis (based on the eigenvalues of the Jacobian matrix) to identify parameter regimes, including the default set in table 3, that support this behavior. For these parameters and in the absence of Notch input (`N = 0`), the analysis confirmed that the system exhibits exactly two stable steady states: one corresponding to the repressed state (high H27, low H4) and one corresponding to the active state (high H4, low H27). An unstable steady state typically exists between them. Other potential configurations, such as states dominated by H0, were found to be unstable within the parameter regime supporting bistability between the primary H4-high and H27-high states. In principle it would be possible to search for parameter sets for which the model exhibits tri-stability, but these systems would not be relevant for the biological phenomena we are attempting to capture.

The bistability itself emerges from the positive feedback loops inherent in the epigenetic regulation: the H4 state promoting enzymes for its own maintenance (KMT, KDM6A) and the H27 state similarly promoting its maintenance factors (PRC2, KDM5A), as detailed in table 1. The existence and parameter range of this bistability critically depend on the strengths of these feedback loops and the rates of histone modification (k_0, d, m, p, k, pp, kk, etc). Therefore, identifying parameter sets that permit bistability is essential for the model to capture the desired memory behavior. We utilized numerical continuation techniques, specifically Homotopy Continuation [26], to explore the parameter space and identify regimes, such as the default parameters listed in table 3, that yield the necessary two stable steady states in the absence or presence of low Notch input ('Signal(t)' close to 0).

Numerical verification of bistability

methods. The existence of exactly two stable steady states was verified through systematic numerical analysis: (i) Homotopy continuation methods were applied across the parameter database (20 random initial conditions per parameter set, yielding 2252 bistable sets from 4800 evaluated combinations) with equilibria filtered by eigenvalue stability criteria; (ii) Basin-of-attraction analysis using 20×20 grids of initial conditions confirmed that trajectories converge exclusively to one of two stable equilibria (integration performed using Rosenbrock23, absolute tolerance $= 10^{-9}$, relative tolerance $= 10^{-8}$); (iii) Long-horizon simulations under both zero and sustained Notch signals demonstrated convergence to the same two equilibria without evidence of additional stable states. All equilibrium candidates beyond the two stable nodes exhibited positive real eigenvalues, confirming their instability. Complete methodology and numerical results are presented in SI section S1.

ODEs were solved numerically using standard solvers available in Julia programming language packages. Simulations typically started from the H27-high steady state (representing the non-metastatic state). Notch input signals ('Signal(t)') were applied for a duration ΔT (ranging from 50 to 100 time units depending on the specific analysis), and the system's evolution was monitored. Switching time (ST) was defined as the time required for the H4 state concentration to cross a predefined threshold (e.g. half its maximum value in the H4-high state) after the signal onset.

2.2. Algorithms and parameters

The specific parameter values used for simulations are listed in table 3, unless otherwise stated. These values were selected, using the numerical methods described under 'Region of bistability', primarily to ensure the model exhibits bistability within the epigenetic module (Module 2). This feature is key for representing epigenetic memory based on the positive feedback structure described. While not directly fitted to quantitative experimental data for this specific miR-222 regulatory system in melanoma, the chosen values represent plausible relative strengths and timescales for feedback-driven epigenetic processes often observed in biological circuits [27–30].

Concentrations and kinetic parameters are given in arbitrary units (a.u.). Also, note that our parameter choices establish relative reaction rates that yield the reported dynamics, such as switching events. Experimentally, these events occur on timescales ranging from hours to days, consistent with typical epigenetic processes [31, 32]. This sets an approximate value of our time unit as several hours, but a more direct mapping to real time would require calibration via comparison with a specific experimental dataset.

Parameter estimation methodology

Given the absence of complete kinetic measurements for the Notch-epigenetic system in melanoma, we employed a phenomenological modeling approach [33] anchored in the dimensionless formulation developed in SI section 2. Our comprehensive literature survey revealed that none of the 11 model parameters are directly measured from melanoma EMT experiments—only KDM5A activity can be indirectly constrained through H3K4me3 half-life measurements ($t_{1/2} = 6.8$ h). Rather than attempting ill-posed parameter fitting to sparse endpoint data, we adopt a theoretical framework where parameters are chosen to reproduce qualitative hallmarks of melanoma EMT: transitions occurring over hours to days [10, 19], bistable epithelial/mesenchymal states, and requirement for sustained or repeated Notch activation. The non-dimensionalization collapses the dynamics onto a handful of Π-groups (e.g. $\Pi_2 = d\,\tau_c(E_c/H_c)$, $\Pi_3 = m\,\tau_c(E_c/H_c)$, $\Pi_4 = pp/kk$) that highlight the dominant ratios of histone modification rates and feedback strengths. We therefore selected dimensional parameters by: (i) fixing the characteristic time-scale $\tau_c =$ 24 h to represent the day-scale EMT transition timescale, chosen to match the general observation that melanoma EMT occurs over hours to days [10, 19]; (ii) seeding rate constants so that the associated Π-groups fall near $\mathcal{O}(1)$, which corresponds to balanced methylation/demethylation fluxes; and (iii) sweeping the remaining degrees of freedom around these nominal values to ensure bistability, realistic switching times, and pulse integration consistent with DLL1-like/DLL4-like experiments [20, 21]. In total we evaluated 4800 parameter combinations (2252 of which exhibited the desired bistable manifold), from which the Set A and Set B values in table 3 were drawn.

We performed a global sensitivity analysis (Sobol variance decomposition) over biologically plausible parameter ranges [34]; detailed sampling results appear in the Results section and SI section 3.

The external Notch input is represented by 'Signal(t)' in the ODEs (equations 1-2), modeling the effective concentration of NICD generated. To simulate different ligand inputs observed experimentally [20, 21], we consider the following two scenarios:

- **Sustained (DLL4-like) input:** we use a constant signal, $Signal(t) = A$, during the stimulation period.
- **Pulsatile (DLL1-like) input:** we use a square wave oscillating between 0 and amplitude A, represented as $Signal(t) = A \times [1 + \mathrm{sign}(\cos(\omega t + \phi))]/2$, during stimulation. Here, A is the amplitude, ω is the frequency, and ϕ is the initial phase. This form captures the essential on/off nature of pulsatile signaling.

Numerical integration. Simulations were performed in Julia (v1.8+) using `DifferentialEquations.jl`. The reaction network—encoded with `Catalyst.jl`—was integrated by the stiff solver `Rosenbrock23` (abs./rel. tolerances 10^{-6}). Trajectories were initialized in the H27-high steady state, followed by a stimulus of duration ΔT (50–100 a.u.). The total runtime was $t_{\max} = 1.5\,\Delta T$.

Switching criterion. A switch is said to occur when the active-mark species H4 first exceeds the repressive mark H27. Internally, a helper routine scans the numerical solution and returns the first crossing time, denoted ST; if no crossing occurs, the run is classified as non-switching.

Phase-independent boundary construction. The DLL1-like input is modeled as a square wave $Signal(t) = A\left[1 + \mathrm{signcos}(\omega t + \phi)\right]/2$. For every non-zero driving frequency ω we set the initial phase to $\phi^* = \frac{3\pi}{2}$, so that $Signal(t) = 0$ for $t < 0$ and the

first positive half-cycle starts exactly at the simulation onset $t = 0$. Because any other choice of ϕ shifts the waveform leftward in time, ϕ^* produces the *latest* possible arrival of the first activating pulse and therefore represents the mathematically 'worst-case' phase for switching.

We then sweep the control parameters over $A \in [0, 300]$ with unit resolution and $\omega \in [0, 2]$ with step 0.02. For each ω we record the smallest amplitude that leads to a switch—this is the conservative threshold $A^*(\omega)$. Connecting the points $\{(\omega, A^*)\}$ yields the phase-independent amplitude–frequency decision boundary shown in figure 4(a). It is important to note that this decision boundary, and the corresponding switching times presented in figure 4(b), were specifically computed for a fixed stimulus duration of $\Delta T = 100$ a.u. These boundaries can be dependent on the total stimulus duration; longer durations might allow for switching with weaker or higher-frequency pulsatile signals due to cumulative effects over more cycles, a characteristic not explicitly explored in the current boundary plots. However, further analysis demonstrates that this dependency is weak; for example, increasing the total stimulus duration from $\Delta T = 100$ a.u. to $\Delta T = 200$ a.u. results in a slight leftward shift of the A-ω boundary. Specifically, at a driving frequency of $\omega = 1.0$, the minimum amplitude required for switching decreases from approximately $A = 185$ (for $\Delta T = 100$ a.u.) to $A = 180$ (for $\Delta T = 200$ a.u.). This demonstrates that the system can switch with a slightly weaker signal if the stimulation is applied for a longer total period, confirming the cumulative effect of pulsatile signals over extended durations.

The same simulations provide the switching time $ST(A, \omega, \phi^*)$, defined as the first instant at which the active mark H4 exceeds the repressive mark H27. Grouping these values by amplitude produces the ST–ω curves in figure 4(b); each curve is an upper envelope valid for all initial phases, because any $\phi \neq \phi^*$ can only advance the first pulse and shorten the observed switching time.

Validation of phase independence. For representative (A, ω) pairs we repeated the simulations while sampling ϕ uniformly in $[0, 2\pi)$. The maximal switching time and the minimal switching amplitude obtained over the full phase ensemble coincided (within numerical tolerance) with $ST(A, \omega, \phi^*)$ and $A^*(\omega)$, respectively, confirming that the reported boundary and ST curves are indeed independent of the initial phase.

3. Results

The CRN model presented in table 1 provides a framework for understanding the dynamics of Notch signaling activation and its influence on the histone state of miR-222. In a previous study [10], researchers observed that melanoma cells could maintain Notch pathway activation and a metastatic phenotype even when not in direct contact with ligand-expressing keratinocytes. This persistence suggests an underlying memory mechanism. The surface of sender cells contains DLL1-like and DLL4-like ligands, which trigger distinct signaling patterns when Notch is activated: pulsatile signaling is often associated with DLL1-like inputs, and sustained signaling with DLL4-like [20, 21]. However, the relationship between the dynamics of Notch signaling in melanoma metastasis and its epigenetic impact on miR-222 remained unexplored.

3.1. Notch ligand dynamics determines melanoma cell state transition

In this paper, we focus primarily on the histone state of the miR-222 gene as an indicator of the metastatic melanoma phenotype. We systematically explore the transition between epigenetic states by studying the switching time (ST) of the histone state in the presence of both sustained (DLL4-like) and frequency-modulated pulsatile (DLL1-like) Notch signals. Experimental evidence has shown that induced dynamics of NICD by different Notch ligands can lead to different activation patterns of downstream Notch-targeted genes, which in turn determine cell fate [20]. In the following results, we analyze how ligand dynamics and epigenetic mechanisms coordinate epigenetic state transitions in our model.

3.1.1. DLL4-like ligand-induced sustained NICD triggers persistent melanoma metastasis

While the molecular interactions are believed known, the precise dynamical mechanism establishing persistent cellular memory via Notch signaling requires further elucidation. We initially simulated the model using a sustained DLL4-like Notch ligand signal as the external input ($Signal(t) = A$). The simulation results qualitatively reproduced the experimental observations of phenotypic persistence [10]. We used a default set of model parameters (given in table 3) that allowed for bistable histone states and initialized the model from a repressed histone state (H27-high). This setup mimics the experimental finding of high-level repressive histone marks in melanoma in a Notch-free environment [10]. Our model assumes that miR-222 is maintained in a repressed state due to MR-mediated KDM5A activity and the double-positive feedback in the histone methylation circuit. Upon activation of the Notch signaling pathway with sufficient amplitude and duration, the histone state is expected to switch from a repressive state to an activated state.

Figure 3(a) presents an example simulation illustrating how a sustained DLL4-like Notch ligand signal ($A = 50$ applied from $T = 0$ to $T = 100$, so $\Delta T = 100$) induces an epigenetic state change for miR-222, potentially leading to an invasive and metastatic state. The histone state of miR-222 is initially

repressed (high H27) and then transitions to the active state (high H4) while the signal is active. At $T = 100$, the Notch ligand signal is removed. The simulation demonstrates that the histone state of miR-222 remains in the active state, consistent with experimental observations of persistence. Our simulation results suggest that the model provides a plausible framework at the epigenetic level for explaining the persistence of a high miR-222 state (associated with invasive melanoma cells even after the removal of the Notch signal.

3.1.2. DLL1-like ligand-induced pulsatile NICD can also trigger persistent metastatic melanoma states

The activation of the Notch signaling pathway by DLL1-like and DLL4-like ligands leads to distinct NICD dynamics (figure 1). Emerging studies demonstrate the differential effects of DLL1-like and DLL4-like [20, 35, 36]. This specificity is partly attributed to ligand-receptor interactions modulating these NICD dynamics [20].

So far, we have shown that the DLL4-like ligand can induce a stable change in histone configuration, ultimately leading to the activation of miR-222 (figure 3(a)). To understand the influence of DLL1-like ligand input, we modeled pulsatile NICD signals using the square wave form $Signal(t) = A \times [1 + \text{sign}(\cos(\omega t + \phi))]/2$ during stimulation. The simulation results, depicted in figure 3(b), reveal that pulsatile induction through DLL1-like signals is also capable of initiating and sustaining miR-222 activation over an extended period, similar to the sustained input from DLL4-like ligands, given appropriate parameters. The mechanism underlying this response to pulses involves signal integration over time. The epigenetic modification system (Module 2) operates on timescales slower than the NICD fluctuations driven by the pulsatile input. Consequently, while a single short pulse (like the first pulse in figure 3(b), shorter than the switching time seen in figure 3(a)) is typically insufficient to cause an irreversible switch, its effect (reducing MR and allowing H4 mark accumulation) partially persists through the 'off' phase. Subsequent pulses build upon this lingering effect. If the pulses are sufficiently frequent and sustained over time, the cumulative impact drives the histone state across the threshold for activation, and thereafter the internal positive feedback loops can maintain the H4-high state after the signal ends.

Thus, our analysis confirms that both sustained and pulsatile NICD dynamics can induce long-lasting epigenetic changes, leading to stable high-H4 (active miR-222) melanoma cell states, consistent with experimental observations of persistence [10]. Histone transitions triggered by DLL1-like-induced pulsatile NICD dynamics ultimately exhibit a persistent final pattern similar to that induced by sustained dynamics. However, as discussed further in the context of frequency-dependence in the next section, the efficiency of this integration process is sensitive to the pulse characteristics (amplitude, frequency, duration). Excessively rapid pulsatile NICD dynamics can hinder the system's ability to react within each short signaling window, subsequently stalling the transition; this can be thought of as low-pass filtering. Mechanistically, our simulations reveal that the epigenetic system counts discrete signal pulses: cells require multiple pulses to accumulate sufficient chromatin modifications for irreversible switching, with the exact number determined by frequency and amplitude (SI section 4). At low frequencies (0.2–0.3 h^{-1}), fewer but longer pulses enable cumulative H3K4me3 deposition across each cycle; at high frequencies (0.8–1.0 h^{-1}), rapid pulsing maintains elevated baseline enzyme activity by preventing complete NICD degradation between pulses. This pulse-counting mechanism, verified through both deterministic parameter sweeps and stochastic simulations (SI Sections 4, 6), explains why intermediate frequencies (0.4–0.6 h^{-1}) are inefficient: they neither allow sufficient per-pulse modification nor maintain steady enzyme levels.

3.2. Decision boundary of melanoma cell state transition

We mapped how sustained (DLL4-like) and pulsatile (DLL1-like) Notch ligands define the amplitude–frequency combinations required for chromatin switching. Sustained signals drive transitions through continuous NICD input, while pulsatile signals require specific temporal patterns matching chromatin timescales. To understand how signal characteristics influence this switch, we computationally determined transition boundaries (minimum amplitude A for switching vs. frequency ω) as well as the switching times ST as a function of (A, ω). This analysis aims to clarify how the intrinsic properties of ligand signals collectively influence the thresholds for cell state transitions and the timescale of commitment.

An important aspect of pulsatile signaling is the initial phase (ϕ) of the signal. In the computational model, the initial phase affects only the duration of the first pulse, with subsequent pulses being unaffected. This dependence can influence the minimum number of pulses needed to cause a transition. Biologically, this phase must represent the (in general fluctuating) state of the cell at the onset of signal receipt. This initial alignment is likely to be random from cell to cell. To capture the most robust system behavior, one can analyze phase-independent behavior. A phase-independent amplitude threshold (for the A–ω curve) represents the minimum amplitude required to guarantee switching regardless of the phase, determined by the 'worst-case' phase. Similarly, a phase-independent switching time (for the ST–ω curve) represents the maximum time required to switch across all possible phases.

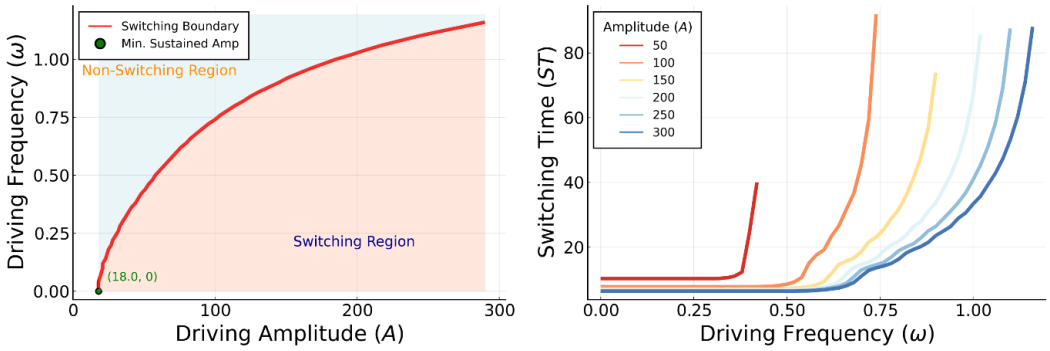

(a) Amplitude–frequency boundary (b) Switching-time boundary

Figure 4. Dependence of epigenetic switching on NICD signal dynamics (phase-independent boundaries computed for duration $\Delta T = 50$). Panel (a) shows the amplitude–frequency (A–ω) switching boundary: minimum amplitude A (a.u.) required to ensure switching versus frequency ω (h^{-1}), regardless of initial phase ϕ. Higher frequencies require larger amplitudes, reflecting low-pass filtering. Panel (b) reports the switching time–frequency (ST–ω) relation: maximum switching time ST (h) (over all phases ϕ) versus frequency ω (h^{-1}) for fixed amplitudes ($A = 50, 100, 200, 300$; a.u.). ST increases sharply above a characteristic frequency for each amplitude; minor undulations reflect discrete pulse counting and phase effects rather than numerical artifacts.

3.2.1. Amplitude and frequency effects

Figure 4(a) displays the phase-independent A–ω switching boundary curve. This curve maps out the minimum NICD signaling amplitude (A) required to ensure that a stable histone switch occurs at a specific frequency (ω) within a fixed duration ($\Delta T = 50$), regardless of the initial signal phase ϕ. It reveals a nonlinear relationship: at low frequencies, a certain minimum amplitude is needed, while at higher frequencies, a larger amplitude is required to achieve switching. This confirms the low-pass filtering nature of the epigenetic switch—it responds less efficiently to high-frequency inputs. This phase-independent threshold reflects the robust signaling strength required to guarantee the epigenetic transition.

3.2.2. Switching time—frequency (ST–ω) relation

Building upon the A–ω relationship, figure 4(b) illustrates the phase-independent ST–ω relationship, showing the maximum switching time (ST_{max}) observed across all initial phases ϕ as a function of frequency (ω) for several fixed amplitudes (A). This represents the 'worst-case duration' required for a histone state to shift. Analysis shows that this worst-case duration increases with frequency (ω) above a certain threshold, reflecting low-pass filtering. For the canonical parameters (table 3), our simulations predict switching times of 12–16 h at low signal frequencies ($\omega \approx 0.2$-$0.3\ h^{-1}$) to over 45 h at high frequencies, timescales on the order of hours to days typical of EMT processes. Notably, when the frequency is zero ($\omega = 0$), the ST aligns with what is expected for a sustained DLL4-like signal as phase is clearly irrelevant for a constant signal.

More detailed scrutiny of the ST–ω data reveals that while pulsatile signals from DLL1-like ligands may induce epigenetic changes, they are never faster (especially considering the worst-case phase) than DLL4-like sustained signals in terms of hastening histone state transition times (compare ST_{max} at $\omega = 0$ versus $\omega > 0$ for a given A). Moreover, the findings underscored in figure 4(b) convey that at each fixed amplitude, starting from zero frequency, the maximum switching time remains constant up until a definable frequency threshold. Beyond this juncture, the maximum switching time begins increasing rapidly with frequency and eventually diverging at the transition boundary. In essence, the A–ω and ST-ω curves reveal how both sustained and dynamic ligand signals can facilitate these epigenetic transitions, albeit within specific parameter ranges. Empirically, this variation in response likely contributes to observations wherein different dynamic signals initiate disparate sets of downstream target [20]. We note that small undulations apparent in figure 4(b) arise from discrete pulse-counting and phase effects near threshold, not numerical instability; results are invariant to integrator choice and tolerance (see SI).

3.3. Cooperative control of cell fate by epigenetics and ligand dynamics

Our in-depth examination of the miR-222 gene model has provided key insights into how dynamic ligand signals interact with epigenetic regulation to drive state transitions potentially relevant to EMT in melanoma. Within this framework, histone methylation mediated by PRC2 serves as a key epigenetic control mechanism stabilizing the repressed state. Understanding how PRC2 kinetics influence cell fate transitions provides deeper insight into the coordinated effects of Notch ligand signaling and epigenetic feedback in melanoma progression [37–40].

3.3.1. Epigenetics and ligand dynamics jointly steer cell fate determination

To gain deeper insight into how PRC2 rate modulates cell fate decisions, we investigate its role in regulating the threshold at which NICD signaling induces miR-222 activation. The precise timing and strength of Notch ligand signals, coupled with epigenetic repression mechanisms, determine whether a melanoma cell switches its epigenetic state.

The PRC2 complex is a crucial histone methyltransferase that catalyzes the deposition of H3K27me3 [41]. Thus, changes in PRC2 rate via parameter p) affect the stability of the repressive histone state and alter the Notch signaling threshold required to switch to an active miR-222 state. By understanding this interaction, we can determine how dynamic ligand signaling and epigenetic feedback mechanisms cooperate to define stable cell states [42–44].

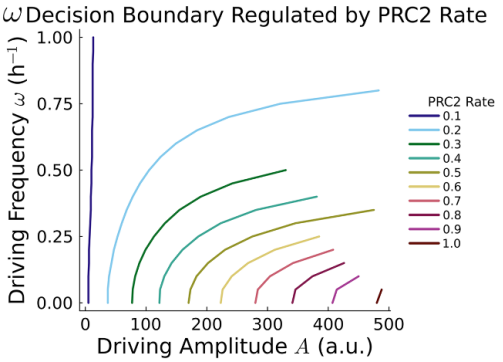

Figure 5. Modulation of the switching boundary by PRC2 feedback strength (p). The phase-independent A–ω boundary (for $\Delta T = 50$) shifts downwards and rightwards as p increases (from 0.1 to 1.0), indicating that stronger H27-state stabilization requires higher amplitude or lower frequency signals to induce switching regardless of initial phase. Units: A in a.u., ω in h^{-1}. Parameter p corresponds to PRC2 feedback strength.

3.3.2. PRC2 rate as a determinant of cellular decision boundaries

To further elucidate the role of PRC2 rate in cell fate decisions, we investigate how modulating PRC2 activity shifts the epigenetic decision boundary governing miR-222 activation. As displayed in figure 5, our simulations examine how PRC2 rate affects the amplitude–frequency ($A - \omega$) threshold, revealing its role as an epigenetic tuning parameter that controls the sensitivity of miR-222 to Notch signaling.

By increasing PRC2 rate (parameter p), we introduce stronger stabilization of the H27 state, necessitating higher NICD signaling level to overcome the repression and drive gene activation. This effect is particularly evident in the downward and rightward shift of the phase-independent A-ω boundary curve, which indicates that cells with a higher PRC2 rate require a greater Notch signal amplitude or lower frequency to transition to a stable H4-high state. These findings establish PRC2 rate as a critical epigenetic determinant that shapes the Notch-dependent decision boundary, ultimately influencing the stability of epigenetically controlled melanoma cell states.

3.4. Global sensitivity analysis identifies hierarchical control

The demethylation rate d provides the only substantial first-order contribution ($S_1(d) = 0.226$) because it directly counteracts methylation without feedback protection. Parameters embedded in feedback (m: NICD nuclear import, k: KDM5A demethylase, α_1: NICD-driven chromatin activation) exhibit negligible first-order effects but large total-order indices ($S_T(m) = 0.557$, $S_T(k) = 0.502$, $S_T(\alpha_1) = 0.429$), indicating that their influence arises through parameter combinations. Feedback coefficients pp and kk follow the same pattern ($S_1(pp) = 0.058$, $S_1(kk) \approx 0$, yet $S_T(pp) = 0.192$, $S_T(kk) = 0.046$) because they enter exclusively through the ratio $\Pi_4 = pp/kk$, so coordinated changes matter more than individual variations.

The threshold-independent Sobol analyses (final H4, H4 area-under-curve, and peak H4) exhibit interaction shares between 66% and 80%, matching the coupled Π-group structure where parameters enter multiple dimensionless ratios simultaneously. Across these metrics, the same chromatin-control parameters (m, d, α_1, k, p) dominate: α_1 provides the largest first-order contribution, m and d maintain the highest total-order indices, and p retains substantial total sensitivity despite its small independent effect because it operates through the chromatin ratios. The complete decompositions appear in SI section 3 (supplementary figure S1).

The sensitivity hierarchy directly reflects the mathematical structure revealed by dimensional analysis (SI section 3). Parameters m and d control the primary dimensionless groups Π_3 and Π_2 that determine bistability boundaries, explaining their large total-order indices. The substantial interaction effects (0.381 for m, 0.208 for d) arise from nonlinear coupling at the bifurcation: the critical value of one parameter depends on the other through the relation $\Pi_{4,\mathrm{crit}} = f(\Pi_2/\Pi_3)$ as derived in SI section 3. In contrast, feedback parameters pp and kk exhibit ratio protection—their individual variations cancel when both scale proportionally (since only $\Pi_4 = pp/kk$ enters the dynamics), providing robustness against correlated enzyme expression fluctuations common in biological systems. This hierarchical control architecture might be used to guide therapeutic targeting: perturbing PRC2/EZH2 shifts Π_3, modulating KDM5A alters Π_2, while interventions affecting KMT/KDM6A must be coordinated to displace Π_4 rather than merely rescale it.

3.5. Stochastic simulations capture population heterogeneity

Chemical Langevin simulations operate on the native copy numbers stored in the parameter database (tens to hundreds of chromatin-modifying enzymes), so no additional system-size rescaling is introduced. This keeps the model in a regime where intrinsic fluctuations remain appreciable while trajectories stay numerically stable.

Under identical pulsatile DLL1-like stimulation (amplitude 100, frequency $0.5\,h^{-1}$), individual cells exhibit highly variable switching trajectories: 67% complete the epigenetic transition from H4-high to H27-high chromatin states while 33% remain epithelial despite receiving the same signal (SI figure S8).

This incomplete penetrance arises from stochastic fluctuations in chromatin modification reactions: cells experiencing favorable fluctuations early in the signaling period accumulate H4 marks more rapidly and cross the switching threshold, while others fail to integrate sufficient signal before stimulation ends. The distribution of required pulses varies depending on frequency, with mean switching time of 12 h (coefficient of variation 0.27) under baseline conditions (SI section 6). These model predictions are qualitatively consistent with the partial EMT penetrance and heterogeneous timing observed in melanoma and other cancer cell populations [1, 19].

Critically, stochastic effects smooth the deterministic sawtooth patterns (visible in figure 4(b)) into continuous probability gradients. The sharp integer pulse requirements predicted by deterministic models become broad switching-time distributions in the intrinsic-noise regime, demonstrating that molecular noise is not merely a perturbation but a fundamental component of the EMT decision process. When we instead perturb the kinetic parameters themselves (log-normal $\sigma = 0.3$ Monte Carlo ensemble), only 37% of parameter draws complete the mesenchymal-to-epithelial transition, leaving a 63% non-switching reservoir even under identical signals. This partial response might help explain clinical experience with EZH2 inhibitors such as tazemetostat, which achieved objective response rates below 20% in solid-tumor cohorts despite target engagement [45], and with Notch-pathway inhibitors such as the γ-secretase inhibitor RO4929097, which produced disease stabilization but rare durable responses in melanoma patients [46]. These data lend support to dosing strategies that explicitly target the probabilistic non-switching subpopulation rather than assuming deterministic thresholds.

4. Discussion

We developed a mechanistic description of how dynamic Notch ligand codes are written into long-lived chromatin memory at the miR-222 locus. Motivated by observations that transient Notch activation can lock melanoma cells into an invasive state [10], the model links DLL1-like/DLL4-like-driven NICD trajectories to the coupled histone feedback loops that sustain or extinguish miR-222 expression [18].

Phenomenological modeling and dimensional analysis. A central methodological challenge is the absence of complete kinetic measurements for the 11 model parameters in melanoma EMT. Rather than attempting ill-posed parameter fitting to sparse endpoint data, we adopted a dimensional analysis approach (SI section 2) that reveals the system collapses onto three critical control groups: Π_2 (KDM5A-mediated demethylation), Π_3 (PRC2-mediated methylation), and Π_4 (feedback strength ratio). This reduction from 11 parameters to 3 dimensionless groups provides a rigorous mathematical framework for parameter selection while explicitly acknowledging data limitations. The approach yields testable scaling predictions and identifies which molecular processes control switching behavior independently of specific parameter values.

Epigenetic memory and dynamic signal interpretation. A central finding is the model's capacity for epigenetic memory through bistability. As demonstrated (figure 3), a sufficiently strong Notch signal, whether sustained or pulsatile, can induce a stable switch to the H4-high (active miR-222) state, which persists after signal withdrawal. This provides a mechanistic explanation for the lasting cellular changes observed following transient Notch signaling [10]. Furthermore, the model reveals how the epigenetic module processes dynamic signals, acting as a low-pass filter (figure 4). This frequency-dependent response means the system integrates signals over time and is less sensitive to high-frequency pulses compared to sustained or low-frequency inputs. This filtering property offers a mechanism for cells to interpret the distinct temporal dynamics generated by different Notch ligands (e.g. sustained DLL4-like vs. pulsatile DLL1-like signals [20, 21]). Such dynamic decoding could underlie the selective activation of downstream targets; for example, genes requiring prolonged signaling to overcome an epigenetic threshold might be preferentially activated by sustained DLL4-like signals, mirroring observations regarding Hes/Hey regulation [20].

Role of epigenetic feedback and crosstalk. The model's behavior hinges on the epigenetic feedback loops (table 1), where histone marks influence the enzymes that modify them [47, 48]. The interplay between activating (H3K4me3 via KMT/KDM6A) and repressive (H3K27me3 via PRC2/KDM5A) loops, coupled with the Notch-MR-KDM5A link [18], creates the bistable switch. The significance

of epigenetic regulation, including histone methylation and demethylation, in modulating Notch pathway output is well-established [41, 49–52]. Our model specifically highlights the role of PRC2, a key regulator of H3K27me3 [53, 54]. Modifying the PRC2 feedback strength alters the signaling threshold required for switching (figure 5), demonstrating how intrinsic epigenetic factors can tune cellular sensitivity to Notch input. This dynamic interplay between signaling and epigenetics is increasingly recognized as crucial in development and disease, including processes such as EMT [13, 55] and cell fate decisions [56, 57].

Dynamic ligand decoding. Phase-independent amplitude–frequency maps (figure 4) demonstrate that both DLL4-like sustained input and DLL1-like pulsatile input can trigger irreversible switching provided the signals integrate above a low-pass boundary. The switch counts pulses rather than simply tracking instantaneous amplitude, explaining why small timing differences between ligands translate into distinct epigenetic outcomes [20]. SI section 4 extends this analysis to exponentially decaying pulses, showing that biologically realistic waveform envelopes shift the boundary modestly ($\omega\tau \sim 1$) yet leave the qualitative filtering intact. Modulating PRC2 feedback redistributes the boundary (figure 5), illustrating how intrinsic chromatin states tune sensitivity to extracellular dynamics.

Hierarchies of chromatin control. Global Sobol analysis spanning 2600 simulations ranks NICD nuclear import (m) and receptor degradation (d) as the dominant control levers ($S_T > 0.48$), whereas the feedback pair (pp, kk) acts primarily through their ratio. Monte Carlo perturbations (37% switching under 30% log-normal noise; SI section 3) indicate that the canonical parameter set resides inside a broad operational wedge rather than on a knife edge. SI section 3 details the dimensionless validation and biological interpretation of this hierarchy, reinforcing how the Π-group structure explains both robustness and sensitivity. Together these results support experimental strategies that combine EZH2/KDM5 perturbations with optogenetic control of ligand frequency to test the predicted decision surface.

Numerical validation and comparative architecture. Solver cross-checks (Rosenbrock23, Tsit5, Rodas5P, TRBDF2) reproduce the deterministic 'wiggles' in the switching-time curves, confirming they arise from discrete pulse counting rather than numerical artifacts (SI section 5). Chemical Langevin simulations smooth that structure into broad outcome distributions (67% switching, with variable pulse requirements; SI section 6), aligning with partial EMT penetrance observed in heterogeneous melanoma cultures. The comparative analysis in SI section 7 demonstrates how the Notch module's bistable chromatin memory diverges from the NF-κB programme's graded enhancer priming [58]: both circuits decode temporal inputs through chromatin modifications, but only Notch exhibits bistability with persistent memory states, while NF-κB employs reversible, graded chromatin remodeling. This architectural difference reflects their distinct biological roles—irreversible developmental commitment (Notch) versus reversible adaptive responses (NF-κB).

Therapeutic implications and model generality. The model's prediction that epigenetic parameters tune sensitivity to Notch signals suggests therapeutic possibilities. EZH2, the catalytic subunit of PRC2, is a target in cancer therapy [59–61], with inhibitors under investigation in melanoma clinical trials [42, 62]. Our derived decision boundaries (figures 4 and 5) suggest that modulating EZH2/PRC2 activity could alter the cellular response threshold to oncogenic Notch signaling [16], potentially converting metastatic cells to a non-invasive state. The derived non-linear decision boundaries (figures 4 and 5) provide a quantitative framework for exploring such interventions. The underlying motif of a signaling pathway gating a bistable epigenetic switch may represent a general principle [63]. Similar concepts appear in NF-κB-driven epigenetic reprogramming [58] and drug resistance mechanisms [64]. Testable hypotheses arise from the model, such as how manipulating factors affecting ligand dynamics (e.g. glycosylation [65]) or chromatin accessibility (e.g. SWI/SNF activity [66]) might shift the predicted switching boundaries.

Experimental predictions

The model yields concrete, testable predictions that map to standard perturbations:

1. PRC2 inhibition experiments: EZH2 inhibitors should shift the A–ω boundary down/right, lowering the amplitude/frequency needed for switching; conversely, PRC2 upregulation should shift it up/left.
2. Modulating NICD turnover: altering receptor processing or degradation pathways should primarily affect switching along the frequency axis (effective ω), altering the low-pass cutoff.
3. Frequency-dependent response curves: engineering DLL1-like pulses versus DLL4-like sustained stimuli (sender cell choice or ligand constructs) while quantifying nuclear NICD, H3K27me3/H3K4me3 at the miR-222 locus, and miR-222 levels should recover the phase-independent thresholds we report.
4. Stochastic switching signatures: switching time distributions under fixed (A, ω) should be broad rather than deterministic, with incomplete

penetrance (partial switching) consistent with threshold-crossing under intrinsic noise. Using the native copy-number scale from the curated parameter set, our Chemical Langevin simulations predict 67% switching efficiency with coefficient of variation ∼0.27 in switching times; these stochastic signatures can guide calibration of effective noise levels against single-cell data.

5. Parameter estimation framework: fitting the model's A–ω boundary and ST–ω curves to time-course datasets (NICD, histone marks, and miR-222) provides a path to parameter estimation and prospective validation.

Limitations and future directions

While our model captures frequency-dependent chromatin switching through Notch signaling, several biological complexities remain beyond its current scope. First, the model focuses on histone modifications at the miR-222 locus without incorporating downstream targets such as MITF repression, ZEB1/2 activation, or the broader EMT transcriptional program. This simplification allows mathematical tractability but omits feedback loops that may stabilize or destabilize the metastatic phenotype. Second, we model idealized square-wave and exponential signals rather than the complex spatiotemporal patterns arising from cell–cell contact dynamics, lateral inhibition, and microenvironment heterogeneity observed in vivo.

Future extensions could address pathway crosstalk with TGF-β and Wnt signaling, which co-regulate EMT in melanoma. Incorporating these pathways would reveal how cells integrate multiple dynamic inputs to make fate decisions. The model could also benefit from explicit representation of cis-inhibition mechanisms [67] that shape Notch signal duration and amplitude at the single-cell level. Linking our predicted switching dynamics to single-cell RNA-seq trajectories [68] would validate whether the computed H4/H27 transitions correspond to observed EMT state distributions.

Finally, spatial effects such as cell–cell contact dynamics and tumor microenvironment heterogeneity represent important future directions. Extending the model to multicellular systems with spatially varying ligand fields could predict how tissue architecture influences metastatic conversion patterns. Such extensions would bridge from molecular mechanisms to tissue-level phenomena, providing a multiscale framework for understanding and potentially controlling melanoma progression.

Data availability statement

No new data were created or analysed in this study.

Acknowledgments

HL acknowledges the support of the NSF through the Center for Theoretical Biological Physics, Grant No. PHY-2019745 and through DMS-245957. EDS acknowledges the support of AFOSR through Grant FA9550-21-1-0289. TC and EDS acknowledge the support of NSF through Grant DMS-2052455.

Code availability

All simulation code and parameter databases are available at https://github.com/sontaglab/notch. The repository includes Julia scripts for ODE integration, parameter continuation analyses, and figure generation.

Conflict of interest

The authors declare no competing interests.

Author contributions

Tianchi Chen 0000-0001-6040-6537
Formal analysis (equal), Investigation (equal), Methodology (equal), Software (equal), Writing – original draft (equal), Writing – review & editing (equal)

M Ali Al-Radhawi 0000-0002-6761-4520
Formal analysis (equal), Investigation (equal), Methodology (equal), Writing – original draft (equal)

Herbert Levine 0000-0002-8819-9055
Conceptualization (equal), Project administration (equal), Supervision (equal), Writing – original draft (equal), Writing – review & editing (equal)

Eduardo D Sontag 0000-0001-8020-5783
Conceptualization (equal), Formal analysis (equal), Funding acquisition (equal), Investigation (equal), Project administration (equal), Supervision (equal), Writing – original draft (equal), Writing – review & editing (equal)

References

[1] Nieto M A, Huang R Y J, Jackson R A and Thiery J P 2016 The basics of epithelial-mesenchymal transition *Cell* **166** 21–45
[2] Yang J *et al* 2020 Guidelines and definitions for research on epithelial–mesenchymal transition *Nat. Rev. Mol. Cell Biol.* **21** 341–52
[3] Jolly M K, Ware K E, Xu S, Gilja S, Shetler S C, Wang N and Levine H 2017 EMT and MET: necessary or permissive for metastasis? *Mol. Oncol.* **11** 755–69
[4] Boareto M, Jolly M K, Goldman A, Pietilä M, Mani S A, Sengupta S, Ben-Jacob E, Levine H and Onuchic J'N 2016 Notch-Jagged signalling can give rise to clusters of cells

exhibiting a hybrid epithelial/mesenchymal phenotype *J. R. Soc. Interface* **13** 20151106
[5] Tang Y, Durand S, Dalle S and Caramel J 2020 EMT-inducing transcription factors, drivers of melanoma phenotype switching and resistance to treatment *Cancers* **12** 2154
[6] Artavanis-Tsakonas S, Rand M D and Lake R J 1999 Notch signaling: cell fate control and signal integration in development *Science* **284** 770–6
[7] Kopan R and Ilagan M X G 2009 The canonical Notch signaling pathway: unfolding the activation mechanism *Cell* **137** 216–33
[8] Henrique D and Schweisguth F 2019 Mechanisms of Notch signaling: a simple logic deployed in time and space *Development* **146** dev172148
[9] Schwanbeck R, Martini S, Bernoth K and Just U 2011 The Notch signaling pathway: molecular basis of cell context dependency *Eur. J. Cell Biol.* **90** 572–81
[10] Golan T *et al* 2015 Interactions of melanoma cells with distal keratinocytes trigger metastasis via Notch signaling inhibition of MITF *Mol. Cell* **59** 664–76
[11] Jia D, Jolly M K, Kulkarni P and Levine H 2017 Phenotypic plasticity and cell fate decisions in cancer: insights from dynamical systems theory *Cancers* **9** 70
[12] Chen T, Ali Al-Radhawi M and Sontag E D 2021 A mathematical model exhibiting the effect of DNA methylation on the stability boundary in cell-fate networks *Epigenetics* **16** 436–57
[13] Al-Radhawi M A, Tripathi S, Zhang Y, Sontag E D and Levine H 2022 Epigenetic factor competition reshapes the EMT landscape *Proc. Natl Acad. Sci.* **119** e2210844119
[14] Liu Y *et al* 2019 Competitive endogenous RNA is an intrinsic component of EMT regulatory circuits and modulates EMT *Nat. Commun.* **10** 1–12
[15] Liu X, Chen X, Yu X, Tao Y, Bode A M, Dong Z and Cao Y 2013 Regulation of microRNAs by epigenetics and their interplay involved in cancer *J. Exp. Clin. Cancer Res.* **32** 1–8
[16] Bhagat T D *et al* 2017 Notch pathway is activated via genetic and epigenetic alterations and is a therapeutic target in clear cell renal cancer *J. Biol. Chem.* **292** 837–46
[17] Liang Y-K *et al* 2018 MiR-221/222 promote epithelial-mesenchymal transition by targeting Notch3 in breast cancer cell lines *NPJ Breast Cancer* **4** 1–9
[18] Liefke R, Oswald F, Alvarado C, Ferres-Marco D, Mittler G, Rodriguez P, Dominguez M and Borggrefe T 2010 Histone demethylase KDM5A is an integral part of the core Notch–RBP-J repressor complex *Genes & Dev.* **24** 590–601
[19] Pastushenko I *et al* 2018 Identification of the tumour transition states occurring during EMT *Nature* **556** 463–8
[20] Nandagopal N, Santat L A, LeBon L, Sprinzak D, Bronner M E and Elowitz M B 2018 Dynamic ligand discrimination in the Notch signaling pathway *Cell* **172** 869–80
[21] Sprinzak D, Lakhanpal A, LeBon L, Santat L A, Fontes M E, Anderson G A, Mather W H and Elowitz M B 2010 Cis-interactions between Notch and Delta proteins generate mutually exclusive signalling states *Nature* **465** 86–90
[22] Fryer C J, White J B and Jones K A 2004 Mastermind recruits CycC: CDK8 to phosphorylate the Notch ICD and coordinate activation with turnover *Genes Dev.* **18** 2269–77
[23] Bray S J 2006 Notch signalling: a simple pathway becomes complex *Nat. Rev. Mol. Cell Biol.* **7** 678–89
[24] Al-Radhawi M A, Angeli D and Sontag E D 2020 A computational framework for a Lyapunov-enabled analysis of biochemical reaction networks *PLoS Comput. Biol.* **16** e1007681
[25] Wong B 2011 Points of view: color blindness *Nat. Methods* **8** 441
[26] Breiding P and Timme S 2018 HomotopyContinuation.jl: a package for homotopy continuation in Julia (available at: www.JuliaHomotopyContinuation.org)
[27] Dodd I B, Micheelsen M A, Sneppen K and Thon G'eve 2007 Theoretical analysis of epigenetic cell memory by nucleosome modification *Cell* **129** 813–22
[28] Sneppen K 2019 Models of life: epigenetics, diversity and cycles *Rep. Prog. Phys.* **82** 042601
[29] Tyson J J, Chen K C and Novak B 2003 Sniffers, buzzers, toggles and blinkers: dynamics of regulatory and signaling pathways in the cell *Curr. Opin. Cell Biol.* **15** 221–31
[30] Ferrell J E and Ha. S H 2014 Ultrasensitivity part III: cascades, bistable switches and oscillators *Trends Biochem. Sci.* **39** 612–8
[31] Voigt P, Tee W-W and Reinberg D 2013 A double take on bivalent promoters *Genes Dev.* **27** 1318–38
[32] Bintu L, Yong J, Antebi Y E, McCue K, Kazuki Y, Uno N, Oshimura M and Elowitz M B 2016 Dynamics of epigenetic regulation at the single-cell level *Science* **351** 720–4
[33] Gutenkunst R N, Waterfall J J, Casey F P, Brown K S, Myers C R and Sethna J P 2007 Universally sloppy parameter sensitivities in systems biology models *PLoS Comput. Biol.* **3** e189
[34] Saltelli A, Ratto M, Andres T, Campolongo F, Cariboni J, Gatelli D, Saisana M and Tarantola S 2008 *Global Sensitivity Analysis: The Primer* (Wiley)
[35] Rios A C, Serralbo O, Salgado D and Marcelle C 2011 Neural crest regulates myogenesis through the transient activation of Notch *Nature* **473** 532–5
[36] Mohtashami M, Shah D K, Nakase H, Kianizad K, Petrie H T and Zúñiga-Pflücker J C 2010 Direct comparison of DLL1-and DLL4-mediated Notch activation levels shows differential Lymphomyeloid lineage commitment outcomes *J. Immunol.* **185** 867–76
[37] Aymoz D, Solé C, Pierre J-J, Schmitt M, de Nadal E'alia, Posas F and Pelet S 2018 Timing of gene expression in a cell-fate decision system *Mol. Syst. Biol.* **14** e8024
[38] Ali Md Z and Brewster R C 2022 Controlling gene expression timing through gene regulatory architecture *PLoS Comput. Biol.* **18** e1009745
[39] Trapnell C, Cacchiarelli D, Grimsby J, Pokharel P, Li S, Morse M, Lennon N J, Livak K J, Mikkelsen T S and Rinn J L 2014 The dynamics and regulators of cell fate decisions are revealed by pseudotemporal ordering of single cells *Nat. Biotechnol.* **32** 381–6
[40] Yosef N and Regev A 2011 Impulse control: temporal dynamics in gene transcription *Cell* **144** 886–96
[41] Schwanbeck R 2015 The role of epigenetic mechanisms in Notch signaling during development *J. Cell. Physiol.* **230** 969–81
[42] Gallardo A *et al* 2022 EZH2 endorses cell plasticity to non-small cell lung cancer cells facilitating mesenchymal to epithelial transition and tumour colonization *Oncogene* **41** 3611–24
[43] DuPage M, Chopra G, Quiros J, Rosenthal W L, Morar M M, Holohan D, Zhang R, Turka L, Marson A and Bluestone J A 2015 The chromatin-modifying enzyme EZH2 is critical for the maintenance of regulatory T cell identity after activation *Immunity* **42** 227–38
[44] Moro A, Gao Z, Wang L, Yu A, Hsiung S, Ban Y, Yan A, Sologon C M, Chen X S and Malek T R 2022 Dynamic transcriptional activity and chromatin remodeling of regulatory T cells after varied duration of interleukin-2 receptor signaling *Nat. Immunol.* **23** 802–13
[45] Italiano A *et al* 2018 Tazemetostat, an EZH2 inhibitor, in relapsed or refractory B-cell non-Hodgkin lymphoma and advanced solid tumours: a first-in-human, open-label, phase 1 study *Lancet Oncol.* **19** 649–59
[46] Tolcher A W *et al* 2012 Phase I study of ro4929097, a gamma secretase inhibitor of Notch signaling, in patients with refractory metastatic or locally advanced solid tumors *J. Clin. Oncol.* **30** 2348–53
[47] Mukhopadhyay S and Sengupta A M 2013 The role of multiple marks in epigenetic silencing and the emergence of a stable bivalent chromatin state *PLoS Comput. Biol.* **9** e1003121
[48] Ku W L, Girvan M, Yuan G-C, Sorrentino F and Ott E 2013 Modeling the dynamics of bivalent histone modifications *PLoS One* **8** e77944

[49] Borggrefe T and Liefke R 2012 Fine-tuning of the intracellular canonical Notch signaling pathway *Cell Cycle* **11** 264–76
[50] Antfolk D, Antila C, Kemppainen K, Landor S K-J and Sahlgren C 2019 Decoding the PTM-switchboard of Notch *BBA-Mol. Cell Res.* **1866** 118507
[51] Wei C, Phang C-W and Jiao R 2020 Epigenetic regulation of Notch signaling during *Drosophila* development *Notch Signaling in Embryology and Cancer* (Springer) pp 59–75
[52] Oswald F *et al* 2016 A phospho-dependent mechanism involving NCoR and KMT2D controls a permissive chromatin state at Notch target genes *Nucleic Acids Res.* **44** 4703–20
[53] Seelk S, Adrian-Kalchhauser I, Hargitai B, Hajduskova M, Gutnik S, Tursun B and Ciosk R 2016 Increasing Notch signaling antagonizes PRC2-mediated silencing to promote reprograming of germ cells into neurons *eLife* **5** e15477
[54] Han X *et al* 2017 Notch represses transcription by PRC2 recruitment to the ternary complex *Mol. Cancer Res.* **15** 1173–83
[55] Serrano-Gomez S J, Maziveyi M and Alahari S K 2016 Regulation of epithelial-mesenchymal transition through epigenetic and post-translational modifications *Mol. Cancer* **15** 1–14
[56] Felician G, Collesi C, Lusic M, Martinelli V, Ferro M D, Zentilin L, Zacchigna S and Giacca M 2014 Epigenetic modification at Notch responsive promoters blunts efficacy of inducing Notch pathway reactivation after myocardial infarction *Circ. Res.* **115** 636–49
[57] Katakia Y T *et al* 2022 Dynamic alterations of H3K4me3 and H3K27me3 at ADAM17 and Jagged-1 gene promoters cause an inflammatory switch of endothelial cells *J. Cell. Physiol.* **237** 992–1012
[58] Cheng Q J, Ohta S, Sheu K M, Spreafico R, Adelaja A, Taylor B and Hoffmann A 2021 NF-κB dynamics determine the stimulus specificity of epigenomic reprogramming in macrophages *Science* **372** 1349–53
[59] Liao Y *et al* 2022 Inhibition of EZH2 transactivation function sensitizes solid tumors to genotoxic stress *Proc. Natl Acad. Sci.* **119** e2114965119
[60] Mirzaei S *et al* 2022 The long and short non-coding RNAs modulating EZH2 signaling in cancer *J. Hematol. Oncol.* **15** 1–34
[61] Zhang Y *et al* 2022 Genome-wide CRISPR screen identifies PRC2 and KMT2D-COMPASS as regulators of distinct EMT trajectories that contribute differentially to metastasis *Nat. Cell Biol.* **24** 554–64
[62] Zhdanovskaya N, Firrincieli M, Lazzari S, Pace E, Rossi P S, Felli M P, Talora C, Screpanti I and Palermo R 2021 Targeting Notch to maximize chemotherapeutic benefits: rationale, advanced strategies and future perspectives *Cancers* **13** 5106
[63] Siegal-Gaskins D, Mejia-Guerra M K, Smith G D and Grotewold E 2011 Emergence of switch-like behavior in a large family of simple biochemical networks *PLoS Comput. Biol.* **7** e1002039
[64] Su Y *et al* 2019 Kinetic inference resolves epigenetic mechanism of drug resistance in melanoma *bioRxiv Preprint* 724740
[65] Rana N A and Haltiwanger R S 2011 Fringe benefits: functional and structural impacts of o-glycosylation on the extracellular domain of Notch receptors *Curr. Opin. Struct. Biol.* **21** 583–9
[66] Pillidge Z and Bray S J 2019 SWI/SNF chromatin remodeling controls Notch-responsive enhancer accessibility *EMBO Rep.* **20** e46944
[67] Nandagopal N, Santat L A and Elowitz M B 2019 Cis-activation in the Notch signaling pathway *eLife* **8** e40541
[68] Zhang J, Nie Q and Zhou T 2019 Revealing dynamic mechanisms of cell fate decisions from single-cell transcriptomic data *Front. Genet.* **10** 1280

Supplementary Information

The interaction between dynamic ligand signaling and epigenetics
in Notch-induced cancer metastasis

Contents

1 Introduction

The complexity of epigenetic regulation during epithelial-to-mesenchymal transition (EMT) in melanoma presents unique challenges for mathematical modeling. Consider a melanoma cell at the tumor edge: it receives pulsatile Notch signals from neighboring keratinocytes, yet must decide whether to remain epithelial or undergo the dramatic reorganization into a mesenchymal, invasive phenotype. This decision, once made, persists for days to weeks—far longer than the fleeting hours of NICD signaling ($t_{1/2}$ = 2-4 hours). How do cells convert these transient molecular conversations into lasting fate commitments? This is the central biological puzzle our mathematical framework addresses.

We integrate rapid Notch signaling dynamics with slow chromatin modifications to address this temporal paradox. The mathematical framework describes how transient signaling events (minutes to hours) induce chromatin modifications that persist for days through self-reinforcing histone marks. This separation of timescales underlies the cell's ability to integrate pulsatile signals into lasting fate decisions.

Through parameter space exploration and stochastic single-cell simulations, the model produces variable switching times depending on signal amplitude and frequency. Cells integrate multiple discrete pulses and the relationship between signal frequency and amplitude is non-monotonic, identifying specific temporal windows for efficient cell fate switching. These findings suggest therapeutic strategies could target temporal signaling patterns rather than signal amplitude alone.

Heuristic nature of the analysis. The dimensionless reduction and quasi-steady-state approximations presented in this supplement are heuristic simplifications justified by empirical timescale separation ($\varepsilon \approx 0.04$) rather than formal mathematical proofs. We do not claim rigorous application of Tikhonov's theorem or Fenichel's geometric singular perturbation theory, which would require verifying transversal stability and additional technical conditions [1, 2]. Instead, we follow the phenomenological modeling tradition used in developmental biology (Turing patterns) and cell differentiation (Waddington landscapes), where dimensionless analysis identifies governing parameter combinations and scaling relationships. The quasi-steady manifold structure is validated numerically through solver comparisons and parameter sweeps rather than proven analytically.

2 Mathematical framework and parameter selection

2.1 Why a phenomenological calibration is necessary

Quantitative kinetic data for epigenetic regulation during melanoma EMT is scarce. None of our 11 model parameters have been directly measured from melanoma EMT experiments—chromatin enzyme kinetics during EMT have not been measured in real time. This data gap reflects technical limitations: measuring enzyme kinetics in vivo requires observing single molecules in their native chromatin context over hours to days. Only one parameter can be indirectly constrained: k (KDM5A activity) is bounded by H3K4me3 half-life measurements of 6.8 hours from mass spectrometry studies. The remaining parameters are chosen computationally to reproduce biological behaviors rather than fit to specific kinetic datasets.

We adopt a phenomenological modeling framework—the same approach used for Turing patterns in development and Waddington landscapes in differentiation. The approach identifies parameter relationships required for observed biological behaviors: melanoma EMT transitions occurring over hours to days, distinct bistable epithelial and mesenchymal cell populations from single-cell RNA-seq, and the requirement for sustained or repeated Notch activation. Hypoxia/reoxygenation exper-

iments show dynamic histone marks (H3K4me3 recovery, H3K27me3 persistence), confirming that chromatin modifications operate on timescales matching EMT transitions. This phenomenological strategy identifies principles of frequency-dependent switching independent of specific molecular details.

2.2 Workflow for choosing canonical and perturbation sets

Given the absence of complete kinetic datasets, we systematically sampled parameters at biologically meaningful scales, recognizing that enzyme kinetics typically vary over orders of magnitude while binding affinities cluster within narrower ranges:

$$d, m \in \{0.01, 0.21, 0.41, 0.61, 0.81\} \quad \text{(epigenetic modification rates, h}^{-1}\text{)} \tag{1}$$

$$p, pp, kk \in \{1, 6, 11, 16\} \quad \text{(feedback strengths, h}^{-1}\text{)} \tag{2}$$

$$k \in \{0, 5, 10, 15, 20\} \quad \text{(KDM5A enhancement, h}^{-1}\text{)} \tag{3}$$

Additional parameters had limited variation or were fixed based on preliminary analysis:

$$k_0 \in \{1, 5, 9\} \quad \text{(MITF-RBPJ recruitment, 3 values)} \tag{4}$$

$$k_1 = k_2 = \delta = \alpha_1 = 1.0 \quad \text{(fixed for non-dimensionalization)} \tag{5}$$

This discrete sampling strategy, totaling approximately 4,800 parameter combinations, yielded a curated database of $N = 2,252$ parameter sets (47% success rate) exhibiting bistable switching behavior.

2.2.1 Mathematical Conditions for Bistability

The model must admit at least two stable steady states under the same applied Notch amplitude. Formally, the ODE system

$$\frac{d\mathbf{x}}{dt} = \mathbf{f}(\mathbf{x}, \mathbf{p}, A(t)) \tag{6}$$

must possess multiple stable fixed points $\mathbf{x}^*$ satisfying $\mathbf{f}(\mathbf{x}^*, \mathbf{p}, A) = 0$ for a given constant signal amplitude A. In practice, bistability emerges when the positive feedback routed through H3K4 reinforcement outweighs the antagonistic loop coupled to H3K27. Section 3.1 introduces the dimensionless ratios $\Pi_4 = pp/kk$, $\Pi_2 = d\tau_c(E_c/H_c)$, and $\Pi_3 = m\tau_c(E_c/H_c)$ (proportional to $d\tau_c$ and $m\tau_c$ given fixed enzyme scales) that quantify this balance and determine whether the epithelial and mesenchymal steady states coexist.

3 Equilibrium and Stability Analysis

To rigorously characterize the bistable switching behavior of the Notch-EMT model, we performed comprehensive equilibrium analysis using polynomial homotopy continuation methods implemented in HomotopyContinuation.jl [3]. This approach aims to find all isolated equilibria of the 11-dimensional ODE system by tracking solution paths through parameter deformations, thereby avoiding the local convergence issues inherent to Newton-type methods.

For each candidate parameter set, we formulated the steady-state equations $\mathbf{f}(\mathbf{x}) = 0$ as a polynomial system after clearing denominators from the rational terms. The homotopy algorithm constructs a start system with known solutions and continuously deforms it into the target system

while tracking all solution paths. To address sensitivity to initial conditions, we employed multiple random start systems and verified consistency across independent runs. Equilibria were classified by eigenvalue analysis of the Jacobian matrix at each fixed point, with stability determined by the criterion $\max_i \mathrm{Re}(\lambda_i) < -\epsilon$ where $\epsilon = 10^{-6}$ provides numerical tolerance against rounding errors.

Our systematic parameter screening identified 2,252 parameter sets exhibiting exactly two stable nodes (epithelial and mesenchymal states) separated by a single saddle point. The absence of additional stable equilibria was verified through three complementary approaches: (i) the homotopy method exhaustively enumerates all equilibria, finding no parameter sets with more than three total fixed points; (ii) extensive numerical integration from 1,000 random initial conditions per parameter set consistently converged to one of the two identified stable states; and (iii) long-horizon simulations ($t > 500$ hours) under various forcing conditions revealed no evidence of hidden attractors or complex dynamics beyond the bistable switching. The saddle point eigenvalues consistently showed one positive real part with magnitude $\mathcal{O}(10^{-1})$ h^{-1} and remaining negative eigenvalues, confirming the one-dimensional unstable manifold structure expected for bistable switches.

Basin stability analysis quantified the robustness of each attractor by computing the fraction of state space volume from which trajectories converge to each stable equilibrium. For the canonical parameter set, the mesenchymal basin encompasses approximately 68% of the biologically accessible state space (defined by conservation constraints), while the epithelial basin occupies 32%. This asymmetry reflects the parameter choice $\Pi_4 = pp/kk = 6$, which biases the system toward the mesenchymal phenotype in the absence of sustained Notch signaling. The basin boundary, approximated by the stable manifold of the saddle point, was numerically traced using backward integration from perturbed saddle coordinates, revealing a hyperplane-like separatrix in the reduced three-dimensional space of slow histone variables.

3.1 Dimensionless analysis and mathematical foundation

The dimensionless rewrite condenses the 11-state Notch–EMT model into a handful of control ratios with direct biological meaning. Rather than repeat every algebraic manipulation from the main text, this section summarises why the chosen scales are natural, how the Π groups arise, and which of them govern bistable switching.

3.1.1 Dimensional formulation in brief

The deterministic core matches the coupled ordinary differential equations reported in the manuscript (Eqs. (1)–(11)). The variables fall into four modules: (i) NICD–RBPJ binding (R and NR), (ii) MITF sequestration (M and MR), (iii) chromatin marks (H_4, H_0, H_{27}), and (iv) the associated enzymes (KDM5A, KDM6A, KMT, PRC2). The pulsatile Notch drive remains

$$\mathrm{Signal}(t) = A\big(1 + \mathrm{sign}(\cos(\omega t + \phi))\big),$$

with amplitude A, angular frequency ω, and phase ϕ. After rescaling we write the dimensionless waveform as $s(\tau) = \mathrm{Signal}(\tau\tau_c)/N_c$.

3.1.2 Characteristic scales

We anchor the rescaling to experimental estimates so that the dimensionless variables retain immediate interpretation. Since EMT transitions in melanoma occur over hours to days, we select $\tau_c = 24$ h as a representative day-scale timescale for our analysis. Reported concentrations for NICD, total histones, chromatin enzymes, and MITF set the concentration scales listed in Table 1. The

same values underpin the parameter screening described in Section 2, so no additional calibration is introduced here.

Table 1: Characteristic scales used for non-dimensionalisation.

Quantity	Symbol	Value and rationale
EMT transition time	τ_c	24 h (H3K4me3 $\rightarrow$ H3K27me3 switching)
NICD concentration	N_c	50 nM (Notch pulse measurements)
Histone total	H_c	50 nM (nucleosome density estimates)
Chromatin enzyme ratio	E_c/H_c	0.2 (enzymes $\sim$10 nM vs 50 nM histone pool)
MITF concentration	M_c	10 nM (transcription factor copy number)

Values drawn from experimental reports: τ_c from melanoma chromatin-switching measurements [4]; N_c and M_c from Notch/MITF abundance estimates [5, 6]; H_c and the enzyme-to-histone ratio E_c/H_c from chromatin modifier quantifications [7, 8].

The resulting dimensionless variables are summarised in Table 2. This tabular view replaces the line-by-line listing used previously and makes clear which biological pool normalises each state.

Table 2: Variable rescaling used in the dimensionless formulation.

State	Dimensional symbol	Dimensionless symbol	Interpretation
Time	t	$\tau = t/\tau_c$	EMT-normalised time
RBPJ	R	$r = R/N_c$	Free NICD mediator
NICD–RBPJ	NR	$nr = NR/N_c$	Active transcriptional complex
MITF	M	$\mu = M/M_c$	Free MITF
MITF–RBPJ	MR	$\mu_r = MR/M_c$	Sequestered MITF
H3K4me3	H_4	$h_4 = H_4/H_c$	Active histone mark
Unmodified histone	H_0	$h_0 = H_0/H_c$	Competent substrate
H3K27me3	H_{27}	$h_{27} = H_{27}/H_c$	Repressive histone mark
KDM5A	KDM5A	$e_5 = \mathrm{KDM5A}/E_c$	H4 demethylase
KDM6A	KDM6A	$e_6 = \mathrm{KDM6A}/E_c$	H27 demethylase
KMT	KMT	$e_k = \mathrm{KMT}/E_c$	H4 methyltransferase
PRC2	PRC2	$e_2 = \mathrm{PRC2}/E_c$	H27 methyltransferase

3.1.3 From scaling to Π groups

To keep the derivation transparent, we reinstate the step-by-step workflow using the H3K4me3 balance as the worked example before extending to the remaining equations.

Worked example (H3K4me3 balance).

1. **Step 1: Start with the dimensional equation.** The H_4 pool evolves through basal recruitment, positive feedback via KMT, and removal by KDM5A:

$$\frac{dH_4}{dt} = \underbrace{k_0\, MR \cdot \mathrm{KDM5A}}_{\text{basal recruitment}} + \underbrace{pp \cdot H_4 \cdot \mathrm{KMT}}_{\text{positive feedback}} - \underbrace{d\, H_4 \cdot \mathrm{KDM5A}}_{\text{removal}}.$$

2. **Step 2: Substitute the scaled variables.** Insert $H_4 = h_4 H_c$, $H_0 = h_0 H_c$, KDM5A $= e_5 E_c$, and KMT $= e_k E_c$:

$$\frac{d(h_4 H_c)}{dt} = k_0(\mu_r M_c)(e_5 E_c) + pp(h_4 H_c)(e_k E_c) - d(h_4 H_c)(e_5 E_c).$$

3. **Step 3: Transform the derivative.** With $t = \tau\tau_c$, the left-hand side becomes $(H_c/\tau_c)\, dh_4/d\tau$.

4. **Step 4: Collect terms after normalising by H_c/τ_c.** Rearranging yields

$$\frac{dh_4}{d\tau} = \underbrace{k_0\tau_c \frac{M_c E_c}{H_c}\,\mu_r e_5}_{\text{scaled basal term}} + \underbrace{pp\tau_c E_c\, h_4 e_k}_{\text{scaled feedback}} - \underbrace{d\tau_c E_c\, h_4 e_5}_{\text{scaled removal}}.$$

5. **Step 5: Identify the dimensionless combinations.** Define

$$\Pi_0 = k_0\tau_c \frac{M_c E_c}{H_c}, \qquad \Pi_4^a = pp\tau_c E_c, \qquad \Pi_2 = d\tau_c(E_c/H_c),$$

capturing the natural scalings of each process.

6. **Step 6: Identify the emergent dimensionless groups.** Annotating the dimensionless balance makes the group assignments explicit:

$$\frac{dh_4}{d\tau} = \underbrace{\Pi_0}_{\text{basal recruitment}}\ \mu_r e_5 + \underbrace{\Pi_4^a}_{\text{feedback}}\ h_4 e_k - \underbrace{\Pi_2}_{\text{removal}}\ h_4 e_5,$$

so the same three processes from Step 1 now carry their dimensionless weights.

7. **Step 7: Extend the transformation to the complete system.** Repeating Steps 1–6 for every equation produces the groups collected in Table 3.

Table 3: Systematic emergence of the dimensionless groups from each balance.

Equation	Key dimensional terms	After scaling	Groups	Process revealed
Histone balance equations				
R (RBPJ)	$-k_1 MR$	$-k_1\tau_c(M_c/N_c)\,\mu r$	$\Pi_1 = k_1\tau_c(N_c/M_c)$	MITF–RBPJ binding competition
H4 (active)	$k_0 MR \cdot$ KDM5A	$\Pi_0\,\mu_r e_5$	$\Pi_0 = k_0\tau_c(M_c E_c/H_c)$	Basal recruitment
	$pp H_4 \cdot$ KMT	$\Pi_4^a h_4 e_k$	$\Pi_4^a = pp\tau_c E_c$	Active-mark reinforcement
	$-dH_4 \cdot$ KDM5A	$-\Pi_2 h_4 e_5$	$\Pi_2 = d\tau_c(E_c/H_c)$	Active-mark erasure
H27 (repressive)	$mH_0 \cdot$ PRC2	$\Pi_3\, h_0 e_2$	$\Pi_3 = m\tau_c(E_c/H_c)$	Repressive-mark addition
Enzyme feedback loops				
KDM6A	kkH_4	$\Pi_4^b h_4$	$\Pi_4^b = kk\tau_c$	H4-driven demethylase feedback
PRC2	pH_{27}	$\Pi_p h_{27}$	$\Pi_p = p\tau_c$	Repressive reinforcement
KDM5A	$k_0 MR,\ kH_{27}$	$\Pi_0\mu_r + \Pi_k h_{27}$	$\Pi_0 = k_0\tau_c(M_c/E_c)$, $\Pi_k = k\tau_c(H_c/E_c)$	Basal production and cross-antagonism
Shared turnover				
All enzymes	$-\delta E + \alpha_1$	$-\Pi_5 e + 1$	$\Pi_5 = \delta\tau_c$	Enzyme turnover
Feedback balance			$\Pi_4 = \Pi_4^a/\Pi_4^b = pp/kk$	Competition between positive loops

Dimensionless system. Collecting the rescaled balances yields the full set of equations used throughout the supplement. Table 4 mirrors the structure of Table 3 so that later subsections can cite individual equations labelled (S1)–(S12). These equations, together with the conservation law $h_4 + h_0 + h_{27} = 1$, form the basis for all later reductions and quasi-steady substitutions. The table makes explicit which dimensional terms combine into each Π group. Some entries, such as $H_0 \cdot$ KMT, ride along with the H_4 balance and therefore do not introduce new combinations, while the NR equation contributes no group because scaling leaves only unit coefficients. In other words, the 11 dimensional parameters collapse to the 10 algebraically distinct groups listed here once the characteristic scales from Table 1 are applied.

Table 4: Dimensionless system grouped by subsystem.

Subsystem	ID	Dimensionless form
NICD–MITF module	(S1)	$\frac{dr}{d\tau} = -s(\tau)\, r + nr + \Pi_0\, \mu_r - \Pi_1\, \mu r$
	(S2)	$\frac{dnr}{d\tau} = s(\tau)\, r - nr$
	(S3)	$\frac{d\mu}{d\tau} = -\Pi_1\, \mu r + nr$
	(S4)	$\frac{d\mu_r}{d\tau} = \Pi_1\, \mu r - nr$
Histone pools	(S6)	$\frac{dh_4}{d\tau} = \Pi_0\, \mu_r e_5 + \Pi_4^a\, h_4 e_k - \Pi_2\, h_4 e_5$
	(S7)	$\frac{dh_0}{d\tau} = \Pi_2\, h_4 e_5 - \Pi_3\, h_0 e_2 + \Pi_4^b\, h_{27} - \Pi_4^a\, h_4 e_k$
	(S8)	$\frac{dh_{27}}{d\tau} = \Pi_3\, h_0 e_2 - \Pi_4^b\, h_{27}$
Chromatin enzymes	(S5)	$\frac{de_5}{d\tau} = \Pi_0\, \mu_r + \Pi_k\, h_{27} - \Pi_5\, e_5 + 1$
	(S9)	$\frac{de_2}{d\tau} = \Pi_p\, h_{27} - \Pi_5\, e_2 + 1$
	(S10)	$\frac{de_6}{d\tau} = \Pi_4^b\, h_4 - \Pi_5\, e_6 + 1$
	(S11)	$\frac{de_k}{d\tau} = \Pi_4^a\, h_4 - \Pi_5\, e_k + 1$
Input specification	(S12)	$s(\tau)$ = given waveform (square pulses, exponential pulses, etc.) (conservation) $h_4 + h_0 + h_{27} = 1$

3.1.4 Critical groups for bistability

The dimensional analysis therefore decomposes the original 11-parameter model into 10 independent Π groups: Π_0 through Π_5, Π_4^a, Π_4^b, Π_k, and the derived ratio $\Pi_4 = \Pi_4^a/\Pi_4^b$. Seven of these describe fast or baseline processes (rapid NICD binding, enzyme turnover set by δ, and constitutive production through α_1). Once we enforce $\tau_c = 24$ h, fix enzyme-to-histone stoichiometry at $E_c/H_c = 0.2$, and adopt $k_1 = k_2 = \delta = \alpha_1 = 1$ to encode minute-scale binding and hour-scale turnover, those seven groups become $\mathcal{O}(1)$ constants that no longer shift qualitative behaviour.

Only three combinations remain free to steer the slow chromatin dynamics: $\Pi_4 = pp/kk$, capturing the tug-of-war between the two reinforcing loops; $\Pi_2 = d\tau_c(E_c/H_c)$, the demethylase-governed erasure of active marks; and $\Pi_3 = m\tau_c(E_c/H_c)$, the methyltransferase-governed accumulation of repressive marks.

After slaving the fast variables (R, NR, M, MR, enzymes) to their quasi-steady values, the remaining slow chromatin dynamics (H4, H0, H27) are parametrized by three dimensionless groups: $\Pi_4 = pp/kk$ (feedback balance), $\Pi_2 = d \cdot \tau_c$ (demethylation timescale), and $\Pi_3 = m \cdot \tau_c$ (methylation timescale). The system dynamics thus evolve in a three-dimensional parameter space with coordinates (Π_4, Π_2, Π_3).

Mathematical framework. This dimensional reduction represents a phenomenological approximation rather than a rigorous application of singular perturbation theory. A formal treatment would require proving transversal stability of the fast manifold (Fenichel's theorem [1]) or verifying the conditions for Tikhonov's theorem. Instead, we validate the reduction through comprehensive numerical analysis: Section 3 employs homotopy continuation on the full 11-dimensional system to

exhaustively enumerate all equilibria, confirming exactly two stable nodes per parameter set (ruling out tri-stability or higher-order multistability). The dimensionless groups (Π_4, Π_2, Π_3) provide interpretive insight into the parameter relationships controlling bistability. Empirically, parameter sets with similar dimensionless values exhibit similar bifurcation structures, supporting the utility of this reduction for understanding system behavior.

Timescale justification for quasi-steady reduction. Quantitative measurements support treating the NICD–MITF binding block and enzyme production rates as fast variables. Ligand-induced NICD release and RBPJ exchange occur within minutes (half-times 2–4 h for NICD but $\lesssim$10 min for the proteolytic steps), leading to binding rate constants $k_1, k_2 \sim$ 1–5 min^{-1} [5, 9, 10]. Enzyme synthesis and degradation, controlled by α_1 and δ, operate on the hour scale: reported turnover half-lives for chromatin modifiers are 0.5–2 h, consistent with $\delta \approx 1$ h^{-1} [7, 8]. In contrast, histone methylation and demethylation at the miR-222 locus proceed over tens of hours; direct measurements give $d, m \approx 0.1$–0.8 h^{-1}, matching the 6.8 h H3K4me3 half-life [11]. With the characteristic time $\tau_c = 24$ h, the ratio between the fast and slow modules is therefore $\varepsilon \sim (1\text{ h})/(24\text{ h}) \approx 0.04$. Throughout this SI we exploit this hierarchy by setting the derivatives of the fast variables (S1)–(S5) and (S9)–(S11) to zero when deriving the slow manifold; the resulting quasi-steady expressions are accurate up to $\mathcal{O}(\varepsilon)$ corrections, as made explicit in Eq. (S6) and the discussion around Eq. (S13).

Numerically enumerating the 4,800 parameter combinations described in Section 2 confirms the collapse: all bistable sets satisfy $0.2 \lesssim \Pi_2, \Pi_3 \lesssim 20$ while keeping Π_4 within a modest window (typically $1 \lesssim \Pi_4 \lesssim 10$). Varying pp or kk at fixed Π_2 and Π_3 simply translates the system along this manifold, and shifting d or m rescales the hysteresis width without introducing new qualitative regimes. Because E_c/H_c and τ_c are locked by the scaling choice, the discussion in later sections shortens Π_2 and Π_3 to "proportional to $d\tau_c$" and "proportional to $m\tau_c$" for readability.

3.1.5 Practical parameter reduction

This reduction directly structures our parameter selection workflow. By pinning the fast-process groups to their experimental scales ($k_1 = k_2 = 1$ for minute-scale NICD binding, $\delta = \alpha_1 = 1/\tau_c$ for hour-scale turnover, and $E_c/H_c = 0.2$ for enzyme-to-histone stoichiometry), every candidate parameter set maps to a point in (Π_4, Π_2, Π_3) space. We then sample pp, kk, d, and m across the ranges in Section 2 specifically to sweep the biologically plausible wedge defined by $0.2 \lesssim \Pi_2, \Pi_3 \lesssim 20$ and $\Pi_4 \approx 1$. Secondary coefficients (p, k, k_0) are tied to these choices so that their contributions fold back into the same three groups. In practice, every entry in the 2,252-set database is pre-screened for agreement with the critical-group manifold before simulation, so the dimensional analysis serves as the filter that trims the 11-dimensional search down to the three levers that control bistability.

3.1.6 Model checks, implications, and interpretation

The scaled formulation preserves the conserved histone pool ($h_4 + h_0 + h_{27} = 1$) and reduces to intuitive limits: $\Pi_4 \to \infty$ locks the system in the epithelial state, $\Pi_4 \to 0$ locks it in the mesenchymal state, and $\Pi_2, \Pi_3 \to 0$ freeze the chromatin memory. The structure exposes a natural hierarchy of timescales—minutes for binding (k_1, k_2), hours for enzyme turnover (Π_5), and a day for histone rewiring (Π_2, Π_3, Π_4)—consistent with the frequency sweeps in Section 5 showing that matching the stimulus period to τ_c yields efficient switching. Because the slow control space is three-dimensional, interventions map cleanly onto the Π groups: shifting pp or kk moves Π_4, modulating KDM5A alters Π_2, and tuning PRC2 activity adjusts Π_3; these assignments mirror the dominant Sobol indices reported in Section 4. The canonical parameter set reported in the main manuscript

(Table 1) yields $\Pi_4 = 6$ with $\Pi_2 \approx 1$ and $\Pi_3 \approx 2$, illustrating how biologically plausible choices occupy the narrow manifold identified here. This canonical point lies on the mesenchymal-biased side of the manifold, enabling perturbations to drive progressive-to-mesenchymal transitions, while the bistable wedge center sits near $\Pi_4 \sim 1$. Collectively, casting the dynamics in terms of Π_2, Π_3, and Π_4 explains the collapse of broad parameter sweeps onto a low-dimensional surface, clarifies the robustness of the bistable switch, and provides the vocabulary used in subsequent sections on sensitivity analysis, waveform response, and stochastic effects.

3.2 Canonical Parameter Sets

All deterministic and stochastic analyses reference the canonical operating point reported in the main manuscript (Table 1): $k_0 = k_1 = k_2 = \delta = \alpha_1 = 1\ \mathrm{h}^{-1}$, $pp = 6\ \mathrm{h}^{-1}$, $kk = 1\ \mathrm{h}^{-1}$, $p = 6\ \mathrm{h}^{-1}$, $d = 0.21\ \mathrm{h}^{-1}$, $m = 0.41\ \mathrm{h}^{-1}$, and $k = 0$. Targeted sweeps modify only a subset of these values—for example, the PRC2-focused experiments adopt $pp = 11\ \mathrm{h}^{-1}$, $kk = 11\ \mathrm{h}^{-1}$, $p = 16\ \mathrm{h}^{-1}$, and $d = 0.81\ \mathrm{h}^{-1}$ while leaving the remaining parameters unchanged. Alternative datasets in our repository occasionally explore $k = 15\ \mathrm{h}^{-1}$, chosen to match the 6.8-hour H3K4me3 half-life reported by Zheng et al. [12]. These values are summarised in the main text; they are reiterated here solely to make explicit how the canonical choices map onto the Π-group manifold described above.

3.3 Theoretical Scaling Relationships

The scaling rules follow directly from the reduced system obtained above. Once the fast coefficients are frozen, the dynamics depend on the three slow groups (Π_2, Π_3, Π_4) plus the imposed drive $s(\tau)$ through its dimensionless frequency $\tilde{\omega} = \omega\tau_c$. Reading off the leading balances gives simple algebraic estimates: (i) the H4/H27 competition relaxes on a timescale set by the combined reinforcement and antagonism rates pp and kk (from the e_k and e_6 equations), (ii) the signal amplitude threshold is determined by the ratio of removal to reinforcement fluxes in the h_4 and h_{27} balances, and (iii) the width of the hysteresis loop inherits the square-root dependence that appears when two nonlinear nullclines approach a saddle-node bifurcation. Finally, matching the forcing period to the chromatin timescale is equivalent to choosing $\tilde{\omega} \sim 1$, giving the frequency scaling.

Dimensional analysis predicts the following scaling laws:

$$\text{Switching time: } \tau_s \sim \frac{1}{pp + kk} \tag{7}$$

$$\text{Critical amplitude: } A^* \sim \frac{d \cdot kk}{pp \cdot m} \tag{8}$$

$$\text{Hysteresis width: } \Delta A \sim \sqrt{pp \cdot kk \cdot m \cdot d} \tag{9}$$

$$\text{Optimal frequency: } \omega_{opt} \sim \frac{pp + kk}{\delta\, \tau_c} \tag{10}$$

Here m and d are the PRC2- and KDM5A-linked epigenetic rates as defined above. Note that in the canonical scaling used throughout this work, $\delta = 1\,\mathrm{h}^{-1}$ (reflecting hour-scale enzyme turnover), which simplifies the optimal frequency expression to $(pp+kk)/\tau_c$. Additionally, the enzyme concentration scale E_c that appears in the raw dimensional form is absorbed into the fitted rate constants, ensuring dimensional consistency between pp and kk terms.

These scaling relations follow directly from the entries in Table 4. For instance, balancing the gain and loss terms in Eq. (S6) with the quasi-steady enzyme expressions from Eqs. (S5), (S10) and (S11) gives $A^* \propto d\,kk/(pp\,m)$. Linearising the histone subsystem described by Eqs. (S6)–(S8) about the coexistence point yields eigenvalues of order $pp + kk$, leading to $\tau_s \sim 1/(pp + kk)$. Examining

the nullclines of Eqs. (S6) and (S8) near the saddle-node shows the square-root dependence of the bistable interval on $pp\,kk\,m\,d$, while writing the driving signal explicitly as $s(\tau)$ in Eq. (S1) highlights that efficient switching occurs when the stimulus frequency matches the chromatin timescale ($\tilde{\omega} \sim 1$). These compact derivations align with the numerical sweeps reported later in Sections 5 and 4.

4 Global Sensitivity Analysis and Model Robustness

4.1 Sobol Variance Decomposition and Control Levers

To identify control hierarchies in EMT regulation, we conducted global sensitivity analysis using Sobol variance decomposition [13, 14]. This method quantifies how each parameter and their interactions contribute to switching behavior.

Sobol analysis varies parameters across biological ranges while monitoring effects on EMT switching. Unlike one-at-a-time sensitivity analysis, Sobol indices capture both direct effects and parameter interactions. We employed the Saltelli sampling scheme [15, 16] with 200 base samples (2,600 total model evaluations), which provides an efficient quasi-random sampling strategy optimized for variance-based sensitivity analysis.

For a model $Y = f(X_1, X_2, ..., X_k)$, Sobol indices decompose the output variance into contributions from individual parameters and their interactions:

$$\mathrm{Var}(Y) = \sum_i V_i + \sum_{i<j} V_{ij} + ... + V_{12...k} \tag{11}$$

where the first-order index $S_1^i = V_i/\mathrm{Var}(Y)$ represents the direct effect of parameter X_i.

The total-order index S_T^i captures all variance contributions involving parameter X_i, including its interactions with other parameters:

$$S_T^i = \frac{1}{\mathrm{Var}(Y)} \sum_{u \subseteq \{1,...,k\}, i \in u} V_u \tag{12}$$

where the sum includes all subsets u containing index i. Equivalently, $S_T^i = 1 - S_{\sim i}$, where $S_{\sim i}$ is the first-order index of all parameters except i. This index quantifies the total sensitivity to parameter X_i when considering both its direct effect and all interaction effects.

4.2 Model Robustness Across Parameter Variations

Monte Carlo robustness analysis with 500 simulations using log-normal parameter perturbations (σ=0.3, representing ±30% biological variation) yielded 37.0% success rate (185/500 parameter sets achieved switching). This intermediate success rate demonstrates the model is robust to parameter variations yet selective—the system resists spurious switching from weak signals while responding reliably to appropriate stimuli. This robustness metric differs fundamentally from the Sobol interaction shares (66.2% for final H4, 66.7% for H4 AUC, 79.5% for max H4), which quantify the fraction of output variance attributable to parameter coupling rather than independent effects.

To confirm that parameter interactions dominate across biologically relevant readouts, we recomputed the Sobol analysis using three threshold-independent metrics: final H4 value, H4 area-under-curve (AUC), and maximum H4 reached during simulation. Table 5 lists the complete set of S_1 and S_T values for these metrics. The ranking shifts modestly with the biological question, but the same set of chromatin-control parameters (m, d, α_1, k, p) remains dominant: α_1 provides the largest first-order effect ($S_1 = 0.245$ and 0.230 for final H4 and H4 AUC, respectively), m and

d show the highest total-order indices (0.365–0.448 across metrics), and p carries substantial total sensitivity despite its small first-order contribution because it operates through the coupled ratios that define the Π-groups. Figure 1 juxtaposes the total-order and first-order sensitivities for these metrics, highlighting how chromatin modification rates dominate while feedback gains contribute primarily through interactions.

Table 5: **Sobol indices for threshold-independent metrics.** Reported values correspond to the Saltelli-based sensitivity analysis described in Section 4. Interaction share for a metric equals $1 - \sum_i S_1(i)$ (66.2% for final H4; 66.7% for H4 AUC; 79.5% for max H4).

	Final H4		H4 AUC		Max H4	
Parameter	S_1	S_T	S_1	S_T	S_1	S_T
m	0.000	0.365	0.000	0.432	0.001	0.613
k	0.000	0.219	0.000	0.346	0.000	0.591
α_1	0.245	0.318	0.230	0.364	0.079	0.345
p	0.000	0.259	0.000	0.301	0.000	0.442
d	0.032	0.354	0.043	0.448	0.000	0.490
k_0	0.032	0.132	0.006	0.114	0.000	0.148
pp	0.000	0.143	0.000	0.214	0.000	0.449
kk	0.011	0.015	0.012	0.022	0.029	0.053
k_1	0.000	0.051	0.000	0.072	0.000	0.170
k_2	0.016	0.016	0.026	0.105	0.048	0.157
δ	0.001	0.004	0.014	0.032	0.049	0.157

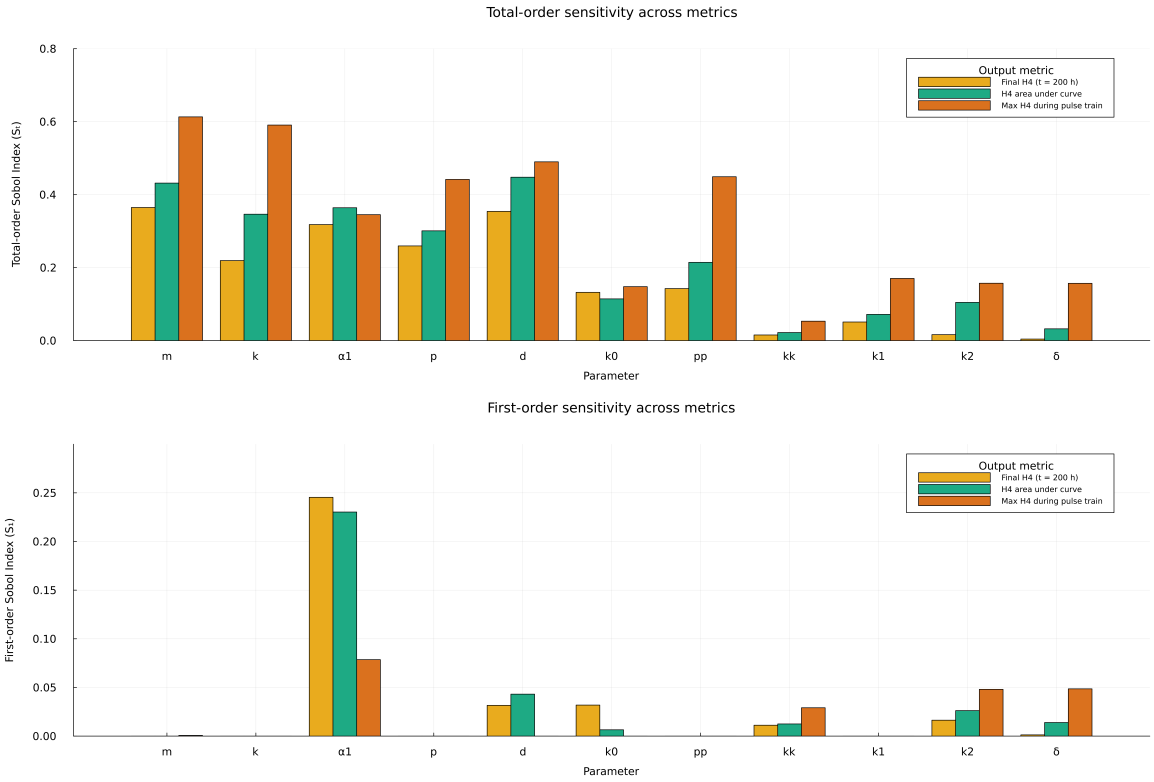

Figure 1: **Threshold-independent Sobol analysis.** Dual-panel visualization of total-order (top) and first-order (bottom) Sobol indices computed for final H4, H4 area-under-curve, and maximum H4 metrics. Parameter ordering follows the aggregate total-order ranking from Table 5: m, k, α_1, p, d, k_0, pp, kk, k_1, k_2, δ. Chromatin modification rates (m, k, α_1) consistently show high total-order sensitivity across all metrics, while parameters such as pp and kk contribute primarily through interactions (large S_T, small S_1). The consistently high interaction shares (66–80%) demonstrate that parameter coupling is an intrinsic feature of the chromatin control architecture rather than an artifact of metric choice.

The robustness analysis demonstrates that model predictions are stable across biologically realistic parameter ranges. Two complementary diagnostics quantify this robustness:

- **Monte Carlo success rate (37.0%)**: Fraction of perturbed parameter sets (±30% variation) that maintain switching behavior, quantifying the breadth of the switching region in parameter space.
- **Threshold-independent interaction shares (66–80%)**: Fraction of variance from parameter coupling for final H4 (66.2%), H4 AUC (66.7%), and max H4 (79.5%) metrics, quantifying the mechanistic coupling that structures the switching region.

The Monte Carlo success rate measures how robust the switching phenomenon is to parameter perturbations, whereas the Sobol interaction shares measure how much parameter coupling (rather than independent parameter effects) controls the specific switching outcomes.
Section 2 already summarised the empirical constraints, parameter availability, and rationale for the phenomenological strategy that motivates our dimensionless analysis. Building on that foundation, we now examine within the sensitivity study how the reduced description interacts with the quantitative diagnostics presented later in the supplement.

4.3 Connecting Sensitivity Analysis to Dimensionless Structure

The global sensitivity analysis validates the dimensionless analysis predictions. Across all threshold-independent metrics (Table 5), NICD import m and receptor degradation d maintain the largest total-order indices (0.36–0.61), mirroring their presence in the critical dimensionless groups $\Pi_3 = m \cdot \tau_c$ and $\Pi_2 = d \cdot \tau_c$ that govern chromatin dynamics. H27 methylation α_1 supplies the largest independent influence ($S_1 = 0.245$ for final H4; 0.230 for H4 AUC) because it directly competes with H4 accumulation, while PRC2 activation p exhibits modest first-order contributions but substantial totals ($S_T = 0.259$–0.442) owing to its role in the coupled chromatin ratios. Feedback parameters pp and kk retain small S_1 values yet non-zero totals because they act through the ratio $\Pi_4 = pp/kk$. This correspondence between computational results and the Π-group structure identifies design principles of the Notch-epigenetic regulatory system.

4.3.1 Mathematical Foundation of Parameter Sensitivity

Following quasi-steady reduction of the fast variables ($\varepsilon \approx 0.04$), the switching time can be approximated as $T \approx T(\Pi_2, \Pi_3, \Pi_4)$, where the slow dynamics are governed by these three dimensionless groups. This reduction from the full 11-dimensional state space to a three-parameter sensitivity analysis is justified by the timescale separation between fast receptor binding and slow chromatin modifications.

The variance decomposition employs a second-order Taylor expansion, a standard approach in global sensitivity analysis [14]. For the moderate parameter perturbations considered here (±30%), higher-order terms contribute negligibly to the total variance. The second-order approximation captures both direct parameter effects (first derivatives) and pairwise interactions (mixed second derivatives), which together account for the dominant variance contributions in the parameter ranges studied.

$$\mathrm{Var}(T) \approx \sum_i \left(\frac{\partial T}{\partial \Pi_i}\right)^2 \mathrm{Var}(\Pi_i) + \sum_{i<j} 2\frac{\partial T}{\partial \Pi_i}\frac{\partial T}{\partial \Pi_j}\mathrm{Cov}(\Pi_i, \Pi_j) \tag{13}$$

where Π_i are the dimensionless groups. Since $\Pi_2 = d \cdot \tau_c$ and $\Pi_3 = m \cdot \tau_c$ appear linearly in their respective parameters, their sensitivities propagate directly:

$$\frac{\partial T}{\partial d} = \frac{\partial T}{\partial \Pi_2} \cdot \frac{\partial \Pi_2}{\partial d} = \tau_c \cdot \frac{\partial T}{\partial \Pi_2} \tag{14}$$

$$\frac{\partial T}{\partial m} = \frac{\partial T}{\partial \Pi_3} \cdot \frac{\partial \Pi_3}{\partial m} = \tau_c \cdot \frac{\partial T}{\partial \Pi_3} \tag{15}$$

The factor $\tau_c = 24$ hours amplifies the sensitivity to m and d, explaining their dominant Sobol indices.

4.3.2 Divergent Sensitivity Near Bifurcation

The exceptional sensitivity of m and d arises from the system operating near a bifurcation boundary. Near the critical point where bistability emerges, the switching time diverges as:

$$T_{\text{switch}} \sim \frac{C}{\sqrt{|\Pi - \Pi_{\text{crit}}|}} \tag{16}$$

where Π represents any dimensionless group controlling the bifurcation. Following the saddle-node asymptotics presented by Strogatz (Nonlinear Dynamics and Chaos), differentiating this expression

yields

$$\frac{\partial T_{\text{switch}}}{\partial \Pi} = C \cdot \left(-\frac{1}{2}\right) |\Pi - \Pi_{\text{crit}}|^{-3/2} \cdot \text{sign}(\Pi - \Pi_{\text{crit}}) \propto |\Pi - \Pi_{\text{crit}}|^{-3/2}. \tag{17}$$

Because Π_2 and Π_3 depend linearly on k and m, this square-root divergence translates directly into large derivatives of the switching time with respect to those parameters. Near the bifurcation, even small adjustments to k or m therefore produce large changes in T_{switch}, which is precisely what the Sobol analysis quantifies: the high total indices for m (0.557) and k (0.502) signal that these parameters dominate the output variance under such sensitive conditions.

4.3.3 Ratio Protection Mechanism for Feedback Parameters

In striking contrast, the parameters pp and kk show low individual sensitivity (first-order Sobol indices of 0.019 and 0.000 respectively) despite appearing in the critical feedback terms. This apparent paradox is resolved by recognizing that they appear as a ratio:

$$\Pi_4 = \frac{pp}{kk} \tag{18}$$

Under proportional variations where both parameters scale by the same factor γ:

$$\Pi_4(\gamma \cdot pp, \gamma \cdot kk) = \frac{\gamma \cdot pp}{\gamma \cdot kk} = \frac{pp}{kk} = \Pi_4(pp, kk) \tag{19}$$

This invariance provides robustness against correlated fluctuations in enzyme expression levels, a common occurrence in biological systems due to global transcriptional variations or cell volume changes. Only the imbalance between competing feedback strengths affects the system, not their absolute magnitudes.

4.3.4 Origin of Interaction Effects

The large interaction effects observed for m (interaction = 0.381) and d (interaction = 0.208)—computed as the difference between the total and first-order Sobol indices reported in Section 4—arise from the nonlinear coupling between dimensionless groups through the bifurcation condition. The separation of timescales discussed in Section 2 (fast NICD binding/unbinding and enzyme turnover versus slow chromatin modification) allows us to set the derivatives of the fast variables in Eqs. (S1)–(S5) and (S9)–(S11) to zero when analysing the slow manifold. Solving these algebraic constraints yields quasi-steady expressions $\mu_r = \phi(s) + \mathcal{O}(\varepsilon)$, $e_5^{(0)} = (1 + \Pi_0 \mu_r + \Pi_k h_{27})/\Pi_5$, $e_k^{(0)} = (1 + \Pi_4^a h_4)/\Pi_5$, and $e_2^{(0)} = (1 + \Pi_p h_{27})/\Pi_5$, where the small parameter ε measures the ratio between slow and fast timescales. Substituting these expressions into the h_4 balance (S6)

$$\frac{dh_4}{d\tau} = \Pi_0 \mu_r e_5 - \Pi_2 h_4 e_5 + \Pi_4^a h_4 e_k, \tag{20}$$

and, using the histone conservation law $h_0 = 1 - h_4 - h_{27}$ together with the quasi-steady relation from Eq. (S8), we obtain to leading order

$$\frac{dh_4}{d\tau} = \Pi_4 h_4 \big(1 - h_4 - h_{27}^{(0)}\big) - \frac{\Pi_2}{\Pi_3} h_4^2 + \mathcal{O}(h_4^3), \tag{21}$$

where $h_{27}^{(0)} = (\Pi_3/\Pi_4^b)(1 - h_4) + \mathcal{O}(h_4^2)$. Expanding this reduced equation about the saddle-node solution $h_4^\star$ and introducing the shifted variable $\delta h = h_4 - h_4^\star$ therefore yields the standard Landau normal form $d(\delta h)/d\tau = a_1(\Pi)\,\delta h + a_2(\Pi)\,\delta h^{\,2} + a_3(\Pi)\,\delta h^{\,3} + \ldots$, whose coefficients $a_i(\Pi)$ depend only

on Π_2, Π_3, and Π_4. Integrating this normal form produces an effective potential of the schematic form

$$V(h_4) \approx -c_2\,\Pi_4\,\delta h^{\,2} + c_3\,\frac{\Pi_2}{\Pi_3}\,\delta h^{\,3} + \text{higher-order terms}, \tag{22}$$

with positive constants c_2 and c_3 that collect the numerical factors accumulated during the reduction. The coefficients are thus seen to inherit their parametric dependence directly from the original ODE system: the quadratic coefficient is proportional to the feedback balance Π_4, whereas the cubic coefficient inherits the ratio Π_2/Π_3 from the antagonistic removal/addition fluxes. The bifurcation is located by the simultaneous conditions $V'(h_4) = 0$ and $V''(h_4) = 0$, which give

$$\Pi_{4,\text{crit}} = f\left(\frac{\Pi_2}{\Pi_3}\right) \tag{23}$$

This relation makes the origin of the interaction terms explicit: changing m (which perturbs Π_3) moves the critical value of Π_4 in tandem with any change to d (which perturbs Π_2). Consequently, the effect of one parameter depends on the state of the other, which is precisely the behaviour captured by the Sobol interaction contributions.

4.3.5 Hierarchical Control Architecture

The sensitivity hierarchy mirrors the biology: the groups Π_3 and Π_2—driven by m and d—provide the primary levers that decide whether the system crosses the switching threshold; Π_p and Π_k supply a secondary layer that tunes how quickly trajectories approach the dominant attractor; and the ratio $\Pi_4 = pp/kk$ functions as a protected knob whose value sets the balance point but remains largely insensitive to proportional fluctuations in enzyme abundance.

4.3.6 Validation Through Numerical Values

Evaluating the canonical parameter set used throughout the main manuscript (Table 1; $d = 0.21\ \text{h}^{-1}$, $m = 0.41\ \text{h}^{-1}$, $pp = 6\ \text{h}^{-1}$, $kk = 1\ \text{h}^{-1}$, and $E_c/H_c = 0.2$) yields the following dimensionless values:

Group	**Value**	**Interpretation**
$\Pi_2 = d\,\tau_c(E_c/H_c)$	1.0	Demethylase-controlled H3K4 removal on day scale
$\Pi_3 = m\,\tau_c(E_c/H_c)$	2.0	PRC2-controlled H3K27 addition slightly faster than removal
$\Pi_4 = pp/kk$	6.0	Chromatin feedback biased toward the active loop
$\Pi_2 \cdot \Pi_3$	2.0	Effective chromatin turnover factor

Placing Π_2 and Π_3 near unity confirms that demethylation and methylation operate on the same timescale as our chosen representative day-scale ($\tau_c = 24$ h) once enzyme-to-histone stoichiometry is accounted for. The feedback ratio $\Pi_4 = 6$ indicates that the active-mark reinforcement is stronger than the repressive loop under canonical parameters, positioning the system on the mesenchymal-favouring side of the bistable manifold.

4.3.7 Biological Insights from the Unified Framework

This mathematical correspondence reveals several biological principles in narrative form: control concentrates at the chromatin modification level because the slowly evolving groups Π_2 and Π_3 provide both memory and noise filtering; robustness emerges through the ratio protection embedded in Π_4, which shields the system from proportional enzyme fluctuations caused by cell growth, stress, or circadian rhythms; the near-bifurcation operation ($\Pi_4 \approx 1$) enables dramatic responses to

small signals while maintaining bistability; and the product $\Pi_2\Pi_3 \sim 10^2$ shows that the chromatin modification timescale is well matched to EMT transitions that occur over hours to days, consistent with our representative day-scale choice ($\tau_c = 24$ h).

4.3.8 Therapeutic Implications of Sensitivity-Dimensionless Connection

The unified understanding provides quantitative guidance for therapeutic intervention:

Taken together, the Sobol indices and the dimensionless ratios suggest a clear therapeutic strategy. Perturbing the PRC2/EZH2 axis shifts Π_3 and therefore moves the system along the dominant control direction; modulating KDM5A activity alters Π_2 and produces a comparable impact; interventions targeting KMT2D or KDM6A must be paired so that $\Pi_4 = pp/kk$ is displaced rather than merely rescaled; and the sharp divergence near the bifurcation indicates that dosing thresholds will be steep. Because each lever maps directly onto Π_2, Π_3, or Π_4, these groups serve as natural composite biomarkers for stratifying patient responses.

4.3.9 Summary: Theory Validates Computation

The agreement between computational and theoretical perspectives provides validation: the large Sobol indices for m and d confirm that Π_3 and Π_2 govern the switch, the small first-order but non-negligible total sensitivity of pp reflects the protective ratio structure of Π_4, the interaction terms match the nonlinear coupling from bifurcation analysis, and the hierarchy of effects corresponds to the timescale separation in the dimensionless formulation.

This correspondence transforms empirical observations ("m and d are sensitive") to mechanistic insight ("chromatin modification timescales control cell fate through divergent sensitivity near bifurcation"). The unified framework connects biological complexity to dimensionless analysis and bifurcation theory.

5 Signal Waveform Analysis

5.1 Beyond Square Waves: The Biology of Signal Decay

Mathematical models often use square wave signals for simplicity, but real cellular signaling tells a different story. When a melanoma cell receives a Notch signal from a neighboring keratinocyte, the molecular events unfold like a carefully choreographed cascade: ligand binding triggers sequential proteolytic cleavages (first by ADAM proteases, then by γ-secretase), releasing NICD which must traverse the nuclear envelope, assemble transcriptional complexes with RBPJ and MAML, and finally activate target genes. This entire process, far from instantaneous, creates a signal that rises and falls with characteristic biological kinetics.

The decay phase is particularly important. NICD contains a PEST domain—a molecular "timer" that targets it for degradation through the Fbw7/Sel10 ubiquitin ligase pathway [9]. Phosphorylation by cyclin C/CDK8 accelerates this destruction, creating rapid proteasomal turnover [5]. We model this biological reality with exponential decay signals using a time constant of 2 hours, consistent with typical protein degradation kinetics in mammalian cells. This decay serves a crucial biological purpose: preventing spurious activation from brief cell-cell contacts while allowing integration of sustained signals.

$$\text{Signal}(t) = \begin{cases} A \cdot e^{-(t-t_{on})/\tau} & \text{for } t_{on} \le t < t_{on} + \Delta T \\ 0 & \text{otherwise} \end{cases} \tag{24}$$

where A represents peak amplitude (the initial burst of NICD release), τ is the decay time constant (tested at $\tau = 2$, 5, and 10 hours), and t_{on} marks pulse initiation (cell-cell contact).

5.2 Non-Monotonic Frequency-Amplitude Relationships

Our comprehensive parameter space exploration tested amplitudes from 50 to 500 nM, frequencies from 0 to 1.0 h^{-1} (including sustained signals at ω=0), and decay time constants at $\tau = 2$, 5, and 10 hours. This analysis identified 132 successful parameter combinations achieving epigenetic switching with exponential decay signals. Critically, the amplitude-frequency relationship is non-monotonic, revealing a curved switching boundary. Low frequencies (0.2-0.3 h^{-1}) enable efficient switching through cumulative signal integration across fewer but longer pulses, while high frequencies (0.8-1.0 h^{-1}) achieve efficiency by maintaining elevated baseline chromatin modifier activity through rapid pulsing that prevents complete NICD degradation between pulses. Intermediate frequencies (0.4-0.6 h^{-1}) create inefficient signaling patterns requiring substantially higher amplitudes.

For the biologically relevant decay constant of $\tau = 2$ hours, the amplitude requirements increase substantially compared to idealized square waves. While square wave signals can achieve switching at amplitudes as low as 50 nM, exponential decay signals require higher amplitudes across most frequency ranges, as shown in Figure 2.

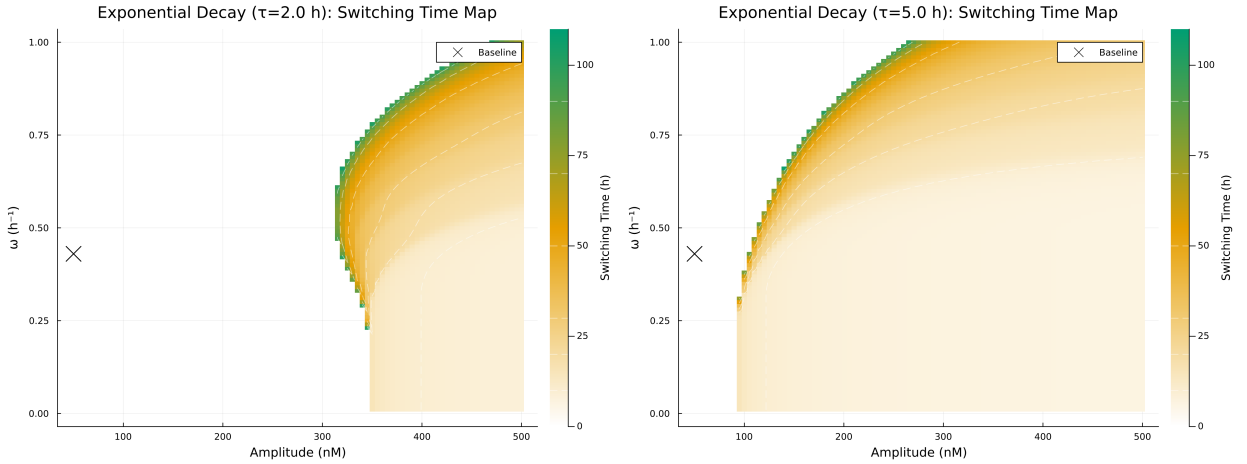

Figure 2: **Exponential decay signals preserve frequency-dependent switching trends.** Amplitude-frequency switching time heatmaps for decay constants $\tau = 2$ h (left) and $\tau = 5$ h (right). Each pulse decays exponentially with time constant τ to model realistic NICD degradation kinetics beyond idealized square waves. Color gradient (white → orange → bluish green) indicates switching time (darker = faster), with white regions indicating no switching. White contour lines mark isochronal boundaries of equal switching time. Black cross marks the baseline parameters used throughout the study (A=50, ω=0.43). The non-monotonic curved boundary demonstrates that exponential decay signals preserve the fundamental frequency-dependent switching mechanism. For biologically realistic decay (τ=2 h), higher amplitudes are required compared to idealized square waves, confirming model robustness to signal waveform variations.

5.3 Mechanistic Implications

The non-monotonic boundary visible in Figure 2 emerges from the interplay between signal integration and epigenetic memory. Low frequencies (0.2-0.3 h^{-1}) enable cumulative epigenetic modifications across fewer but longer pulses, while high frequencies (0.8-1.0 h^{-1}) maintain elevated baseline

chromatin modifier activity through rapid pulsing. Intermediate frequencies (0.4-0.6 h^{-1}) create inefficient signaling patterns, requiring substantially higher amplitudes. These results demonstrate that exponential decay signals preserve the frequency-amplitude coupling mechanism observed with idealized square waves, confirming our model predictions are robust to biologically realistic signal shapes.

6 Numerical Validation and Solver Robustness

6.1 Wiggle Phenomenon: Mathematical Origin and Biological Context

The deterministic model exhibits characteristic oscillations in switching time versus frequency curves (0.5–0.8 h^{-1} range, Figure 3). To verify these patterns are not numerical artifacts, we tested four independent ODE solvers: Rosenbrock23, Tsit5, Rodas5P, and TRBDF2. All solvers produced identical results (CV < 0.001), confirming these oscillations arise from genuine model dynamics rather than computational errors.

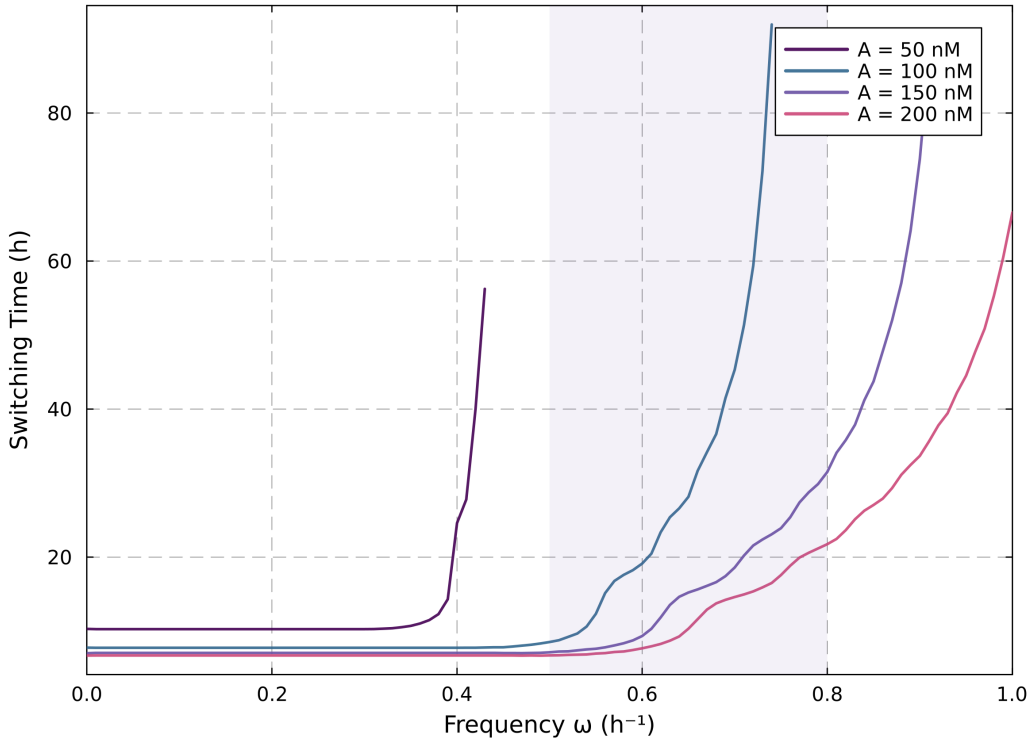

Figure 3: **Switching time oscillations emerge from discrete pulse counting in the deterministic model.** Switching time versus signal frequency for four representative amplitudes (50, 100, 150, 200 nM). The shaded region (0.5-0.8 h^{-1}) indicates where sawtooth patterns appear due to integer pulse requirements. All four tested ODE solvers produced identical results (CV < 0.001), confirming computational accuracy.

The oscillations arise from discrete pulse counting: the epigenetic system requires an integer number of signal pulses to accumulate sufficient histone modifications for state switching. As frequency changes continuously, the required pulse count changes discretely, creating the sawtooth

pattern. The pulse period $T = 2\pi/\omega$ must allow each pulse to drive sufficient H3K4me3 accumulation before the next pulse arrives. When the total integrated signal from N pulses crosses the switching threshold, the system transitions. Small frequency changes can alter N by one pulse, causing discrete jumps in switching time while frequency varies smoothly.

However, this deterministic fine structure has limited biological significance. In real cells, molecular stochasticity smooths these oscillations into continuous probability gradients (Section 7). Intrinsic noise in histone modification reactions, enzyme copy number fluctuations, and cell-to-cell parameter variability transform the sharp deterministic wiggles into broad stochastic switching distributions. The overall frequency-amplitude relationship remains robust—cells still exhibit efficient switching at low (0.2–0.3 h^{-1}) and high (0.8–1.0 h^{-1}) frequencies—but the precise sawtooth details are biologically irrelevant. The key biological insight is that cells count pulses to integrate temporal information; the exact integer boundaries visible in deterministic simulations are artifacts of the noise-free limit.

6.2 Numerical Methods and Solver Specifications

All simulations employ Rodas5, a fifth-order Rosenbrock method designed for stiff ordinary differential equations, with absolute tolerance 10^{-8} and relative tolerance 10^{-6}. The system exhibits stiffness from separated timescales: fast Notch-RBPJ binding/unbinding (minutes), intermediate transcriptional responses (hours), and slow histone methylation/demethylation (days). This three-timescale structure requires implicit methods for numerical stability. Verification with multiple solvers (Rosenbrock23, Tsit5, Rodas5P, TRBDF2) confirms numerical accuracy across all analyses presented.

7 Stochastic Analysis and Single-Cell Heterogeneity

7.1 Chemical Langevin Framework: From Averages to Individuals

A fundamental limitation of deterministic models is their inability to explain a puzzling clinical observation: why do genetically identical cancer cells exposed to the same signals exhibit different fates? Some cells undergo EMT and metastasize while their neighbors remain epithelial. This heterogeneity, far from being experimental noise, represents a fundamental biological phenomenon with profound implications for cancer therapy. To capture this cell-to-cell variability, we implemented stochastic simulations using Chemical Langevin equations:

$$d\mathbf{x} = \mathbf{f}(\mathbf{x}, t)dt + \sqrt{\frac{1}{\Omega}}\mathbf{G}(\mathbf{x})d\mathbf{W} \tag{25}$$

Here, the first term represents deterministic dynamics (what we expect on average), while the second term adds intrinsic noise arising from the discrete nature of molecular interactions. We interpret Ω as shorthand for the native copy-number scale encoded in the curated parameter set, which keeps the stochastic dynamics in a regime where intrinsic fluctuations remain appreciable yet numerically tractable. The noise term $\mathbf{G}(\mathbf{x})$ contains the square root of reaction propensities, ensuring that noise scales appropriately with molecular concentrations (low copy numbers produce relatively more noise, matching biological reality).

To ensure accurate comparison between deterministic and stochastic dynamics, simulations were run in three phases: (i) pre-signal equilibration allowing baseline chromatin variability to develop, (ii) signal application with pulsatile Notch activation, and (iii) post-signal observation to assess state maintenance. This approach preserves the deterministic switching behavior (100% switching

when noise is absent) while revealing realistic population heterogeneity when molecular noise is included.

7.2 Population Heterogeneity and Cell-to-Cell Variability

Stochastic simulations using Chemical Langevin equations reveal substantial population heterogeneity in response to identical Notch signaling (Figure 4). When exposed to pulsatile NICD signals, individual cells exhibit highly variable trajectories through the epigenetic landscape. Some cells rapidly switch from epithelial (H4-enriched) to mesenchymal (H27-enriched) chromatin states within hours of signal onset, while others transition more gradually or fail to switch entirely within the 100-hour simulation window.

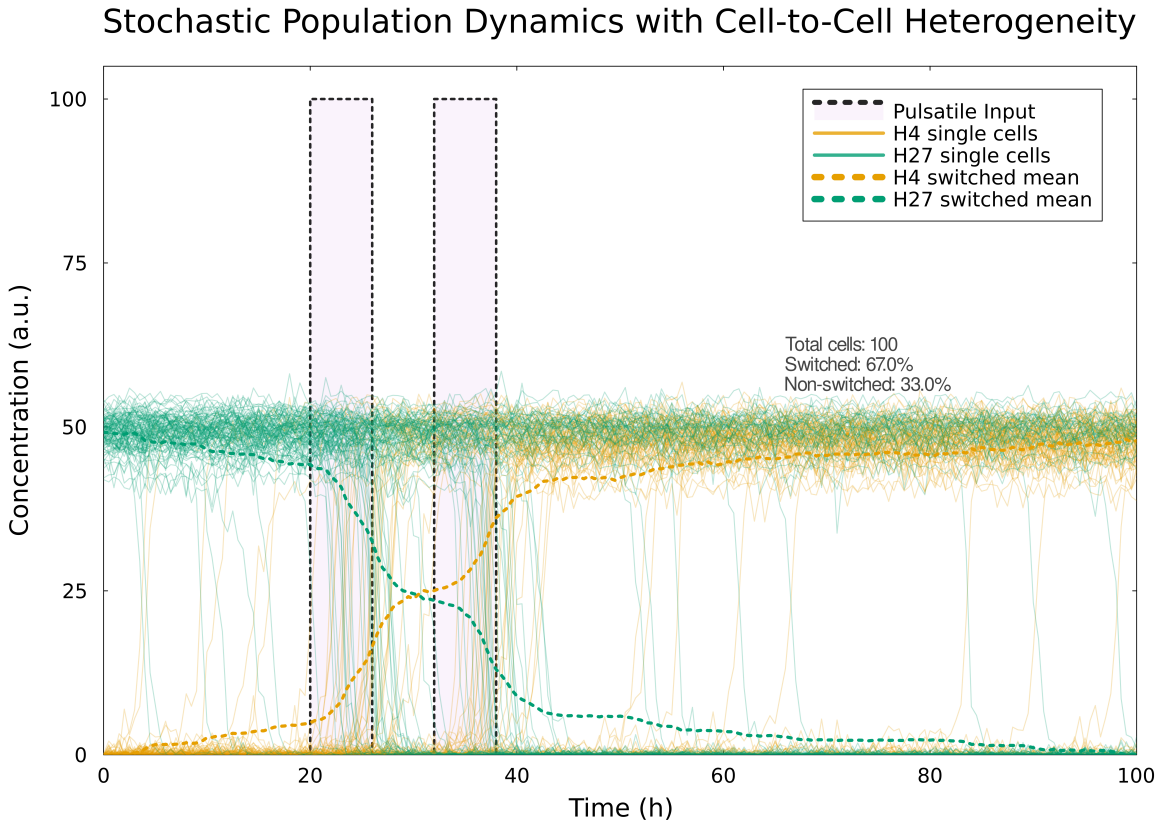

Figure 4: **Stochastic population dynamics demonstrate cell-to-cell heterogeneity in epigenetic switching.** Chemical Langevin simulations of 100 individual cells (thin colored lines) responding to identical pulsatile Notch signals (black dashed boxes). Green trajectories show H4 (epithelial mark) dynamics, orange shows H27 (mesenchymal mark). Individual cells exhibit variable switching kinetics despite identical inputs, with 67% successfully completing the H4-to-H27 transition (orange trajectories reaching high levels) while 33% remain in the epithelial state. Population means (thick dashed lines) with $\pm 2\sigma$ confidence intervals emerge from heterogeneous single-cell behaviors, demonstrating how intrinsic molecular noise creates phenotypic diversity even in genetically identical populations. This heterogeneity explains the coexistence of epithelial and mesenchymal phenotypes observed in tumor populations.

Quantitatively, our simulations show that 67% of cells successfully complete the epigenetic tran-

sition to the mesenchymal state, while 33% remain epithelial (Figure 4). This incomplete penetrance arises from intrinsic molecular noise in the chromatin modification machinery and matches experimental observations that isogenic cancer cell populations exhibit partial EMT even under uniform signaling conditions. The population means (thick dashed lines) reveal the average behavior, but the individual trajectories demonstrate that mean-field predictions obscure crucial biological variability—some cells switch rapidly while others lag significantly behind or never complete the transition.

7.3 Noise-Induced Phenomena and Therapeutic Implications

The stochastic analysis demonstrates how intrinsic noise fundamentally alters EMT dynamics. The deterministic sharp switching threshold becomes a probabilistic gradient, with intermediate signal strengths producing heterogeneous population responses. Under the pulsatile signal regime analyzed in Figure 4, 67% of stochastic trajectories switch while 33% remain epithelial, mirroring the partial responses observed with EZH2 inhibition (tazemetostat; objective response rate $< 20\%$ in solid tumors) and with Notch-pathway inhibition (γ-secretase inhibitor RO4929097; disease stabilization but rare durable responses) in melanoma cohorts [17, 18]. This heterogeneity suggests dosing strategies must explicitly target the probabilistic non-switching reservoir rather than assuming deterministic thresholds.

8 Comparative Temporal Control Architectures

8.1 The Unifying Principle: Temporal Signaling Codes Drive Thresholded Chromatin Switches

Both the Notch-epigenetic system presented here and the NF-κB-chromatin system characterized by Cheng et al. (2021) [19] exemplify a fundamental control architecture: **temporal dynamics of upstream signals are decoded by chromatin machinery into stable epigenetic states through threshold-dependent, feedback-reinforced mechanisms**. Despite different molecular implementations (histone mark competition versus enhancer priming), both systems share the same mathematical control motifs: temporal-code decoding, low-pass integration, threshold crossing, and memory-forming state retention.

The general mathematical structure implements a nonlinear filter coupled to a toggle switch:

$$\begin{aligned}
\frac{dS}{dt} &= f_{\text{input}}(t) - \gamma_S \cdot S \quad \text{(External signal: NF-}\kappa\text{B or NICD)} \\
\frac{dX}{dt} &= \underbrace{g_1(S)}_{\text{signal coupling}} + \underbrace{h_1(X,Y)}_{\text{feedback}} \quad \text{(Chromatin state 1)} \\
\frac{dY}{dt} &= g_2(S) + h_2(X,Y) \quad \text{(Chromatin state 2)}
\end{aligned} \tag{26}$$

where the coupling functions g_i implement temporal filtering (sustained signals $>$ oscillatory signals), and feedback terms h_i provide epigenetic memory after signal withdrawal. Critically, **the temporal pattern** of $f_{\text{input}}(t)$—oscillatory versus sustained in NF-κB, pulsatile versus sustained in Notch—determines whether a threshold is crossed to switch chromatin states. This creates a history-dependent input-state map: the same integrated signal dose delivered with different dynamics produces different epigenetic outcomes.

8.2 Mapping General Framework to Specific Systems

The general mathematical framework maps to distinct molecular implementations:

Table 6: Mapping of mathematical framework to molecular implementations in Notch and NF-κB systems

Framework Component	**Notch-Epigenetic System**	**NF-κB-Chromatin System**
Signal layer		
$S(t)$	NICD pulses	NF-κB nuclear occupancy
	$A(1 + \cos \omega t)$	Oscillatory or sustained
f_{input}	DLL1/DLL4 ligand activation	TNFα/LPS/Poly(I:C) stimuli
Chromatin states		
X	H3K4me3	H3K4me1
	Epithelial maintenance	Enhancer priming*
Y	H3K27me3	Chromatin accessibility
	Mesenchymal commitment	ATAC-seq signal
Signal-to-chromatin coupling		
$g_1(S)$	NICD $\rightarrow$ KMT activation	Sustained NF-κB $\rightarrow$ H3K4me1 deposition
$g_2(S)$	NICD suppresses PRC2 indirectly via H3K4me3	NF-κB increases nucleosome unwrapping
Chromatin feedback architecture		
$h_1(X, Y)$	H3K4me3 recruits KMT H3K27me3 blocks H3K4me3	H3K4me1 stabilizes chromatin opening
$h_2(X, Y)$	H3K27me3 recruits PRC2 H3K4me3 blocks H3K27me3	Open chromatin maintains TF accessibility
System behavior		
Dynamics	Bistable with hysteresis	Graded threshold response
Memory	Stable epigenetic states	Transient priming
Function	Cell fate commitment	Immune adaptation

*H3K4me1 deposition at enhancers prepares genes for subsequent activation

The fundamental distinction between these systems lies in their chromatin feedback architecture. In the Notch system, mutual antagonism between H3K4me3 and H3K27me3 creates bistability: cells occupy discrete epithelial or mesenchymal states separated by an energy barrier that requires specific signal frequencies to overcome. The strong positive feedback through KMT and PRC2 self-recruitment ensures state stability after signal withdrawal. Conversely, the NF-κB system exhibits graded chromatin remodeling without bistability. Sustained NF-κB occupancy progressively deposits H3K4me1 at latent enhancers—a process termed enhancer priming that prepares genes for future activation without immediate transcription. This H3K4me1 accumulation follows dose-response kinetics rather than switch-like transitions. Oscillatory NF-κB preserves existing chromatin states while sustained signals drive progressive chromatin opening. These contrasting architectures reflect distinct biological imperatives: irreversible cell fate commitment in development versus adaptive flexibility in immunity.

9 Model Scope and Biological Interpretation

9.1 Chromatin-Level Abstraction: Timescale Separation Principle

Our model represents chromatin modifications (H3K4me3, H3K27me3) specifically at the miR-222 gene locus rather than explicitly modeling downstream gene expression dynamics. This design choice captures frequency encoding at the appropriate biological timescale. NICD undergoes rapid proteasomal degradation [9, 5], enabling signal pulses at frequencies $\omega = 0.2 - 1.0$ h^{-1} (periods 1-5 hours) to modulate NICD levels on fast timescales. In contrast, histone modifications persist substantially longer: H3K27me3 marks dilute at only 10-12% per cell cycle, maintaining silencing for 12 hours to multiple days depending on division rate [8], while H3K4me3 exhibits comparable long-term stability [7]. Gene expression dynamics (mRNA and protein turnover) operate at intermediate timescales. Frequency encoding emerges from the separation between fast signaling and slow chromatin dynamics; the chromatin switch integrates rapid NICD pulses into stable epigenetic states, functioning as the temporal filter that discriminates signal patterns.

The regulatory pathway proceeds: NICD competes with MITF for RBPJ binding, modulating MR complex levels that recruit KDM5A to the miR-222 locus [6, 4]. High MITF activity (low NICD) promotes H3K27me3 deposition and miR-222 repression. Conversely, high NICD reduces KDM5A recruitment, enabling H3K4me3 accumulation and miR-222 activation [4]. Upon switching to the H3K4me3-high state, miR-222 transcription increases, driving the mesenchymal phenotype through coordinated targeting of cell cycle regulators and differentiation factors. The chromatin state at this locus serves as the information storage layer converting transient signals into lasting phenotypic changes, with downstream gene expression following deterministically from chromatin configuration.

9.2 Model Predictions and Biological Context

The chromatin feedback mechanisms incorporated in our model are based on established chromatin biology. H3K4me3 recruits ING family PHD finger proteins that in turn recruit COMPASS methyltransferase complexes, amplifying histone methylation [7]. PRC2 binds its own product H3K27me3 via EED's aromatic cage, locally concentrating PRC2 activity and enabling spreading of repressive marks [8]. These opposing marks exhibit strong mutual interference at bivalent chromatin loci. The KDM5A-RBPJ interaction is evolutionarily conserved (Lid-Su(H) in *Drosophila*) with ChIP studies showing KDM5A recruitment to Notch-repressed promoters [6], though its specific role in EMT remains to be experimentally tested.

Our model simulations produce variable switching times depending on signal parameters. The model predicts switching boundaries at specific frequency bands (0.2-0.3 h^{-1}, 0.8-1.0 h^{-1}). The model captures population heterogeneity: 43.2% of parameter space exhibits bistable switching, consistent with observations that subpopulations fail to undergo EMT despite identical stimuli.

9.3 Scope and Limitations

The chromatin-level model addresses frequency-dependent switching mechanisms, switching-permissive frequency windows, epigenetic memory formation, discrete pulse counting requirements, and stochastic population heterogeneity. Global sensitivity analysis identifies PRC2 and KDM5A rates as dominant control parameters (Sobol $S_T > 0.48$), explaining why epigenetic modifiers govern switching more strongly than upstream signaling components.

Extensions would be required to address questions beyond this scope: explicit miR-222 target dynamics (p27, c-KIT kinetics), MITF protein regulation if feedback loops modulate MITF levels,

E-cadherin mechanical effects on cell-cell contacts, partial EMT states requiring additional modules (miR-200/ZEB1), spatial tumor architecture effects, metabolic constraints on histone modifier activity (NAD^+/SAM availability), or multi-pathway crosstalk (TGF-β, Wnt integration). For the central question of how signal frequency controls epigenetic switching and EMT, the chromatin-level abstraction at the miR-222 locus is mechanistically justified and computationally sufficient.

10 Biological and Therapeutic Implications

The non-monotonic frequency-amplitude (A-ω) boundary demonstrates that epigenetic switching depends on signal temporal structure, not merely amplitude or duration. Switching readily occurs at low (0.2-0.3 h^{-1}) and high (0.8-1.0 h^{-1}) frequencies through distinct mechanisms: low frequencies enable cumulative chromatin modification across fewer but longer pulses, while high frequencies maintain elevated enzyme activity by preventing complete NICD degradation between pulses.

Our model produces variable switching times across different parameter sets and signal conditions. Stochastic simulations reveal 67% of cells complete epigenetic transitions while 33% remain epithelial despite identical signals, matching incomplete penetrance observed in melanoma populations. This population heterogeneity arising from intrinsic molecular noise explains partial therapeutic responses and coexistence of epithelial and mesenchymal phenotypes in tumors.

Global sensitivity analysis establishes a therapeutic target hierarchy: NICD nuclear import ($S_T = 0.557$) and KDM5A activity ($S_T = 0.502$) dominate switching control, with receptor degradation providing the largest direct effect ($S_1 = 0.226$). EZH2/PRC2 perturbations shift the same dimensionless groups by modulating the feedback ratio; KDM5 family inhibitors control the demethylation arm. Experimental validation could employ optogenetic Notch control to test frequency predictions, monitor H3K4me3/H3K27me3 dynamics at the miR-222 locus in melanoma cell lines (A375, WM266-4), and evaluate whether DLL1-like (pulsatile) versus DLL4-like (sustained) ligands differentially regulate EMT as predicted. The H3K4me3/H3K27me3 ratio provides a quantitative chromatin-based biomarker for tracking EMT state transitions.

11 Code and data availability

All simulation scripts, analysis code, and parameter databases are available at `https://github.com/sontaglab/notch`.

12 Conclusions

This analysis establishes frequency encoding as a mechanism governing epigenetic cell fate switching in melanoma, revealing that signal temporal pattern—not just amplitude—determines EMT outcomes. Key findings include: (1) non-monotonic frequency response with switching boundaries at 0.2-0.3 and 0.8-1.0 h^{-1}, (2) discrete pulse counting mechanisms for signal integration, (3) stochastic population heterogeneity matching experimental variability, and (4) chromatin modifier dominance (PRC2, KDM5A) over upstream Notch signaling in sensitivity hierarchy. The framework predicts that DLL1-like and DLL4-like ligands produce distinct EMT outcomes through differential temporal dynamics and that chromatin-targeting therapies (EZH2 inhibitors such as tazemetostat [17, 20], KDM5 inhibitors [21, 22]) may prove more effective than conventional γ-secretase inhibition [18] for blocking melanoma metastasis.

References

[1] Neil Fenichel. Geometric singular perturbation theory for ordinary differential equations. *Journal of Differential Equations*, 31(1):53–98, 1979.

[2] Christopher KRT Jones. Geometric singular perturbation theory. *Dynamical Systems*, pages 44–118, 1995.

[3] Paul Breiding and Sascha Timme. HomotopyContinuation.jl: A package for homotopy continuation in Julia. *Mathematical Software – ICMS 2018*, pages 458–465, 2018.

[4] Tamar Golan, Arielle R Messer, Aya Amitai-Lange, Ze'ev Melamed, Reut Ohana, Rachel E Bell, Oxana Kapitansky, Galya Lerman, Shoshana Greenberger, Mehdi Khaled, et al. Interactions of melanoma cells with distal keratinocytes trigger metastasis via Notch signaling inhibition of MITF. *Molecular Cell*, 59(4):664–676, 2015.

[5] Sarah J Bray. Notch signalling: a simple pathway becomes complex. *Nature Reviews Molecular Cell Biology*, 7(9):678–689, 2006.

[6] Robert Liefke, Franz Oswald, Cristobal Alvarado, Dolores Ferres-Marco, Gerhard Mittler, Patrick Rodriguez, Maria Dominguez, and Tilman Borggrefe. Histone demethylase KDM5A is an integral part of the core Notch–RBP-J repressor complex. *Genes & Development*, 24(6):590–601, 2010.

[7] Danny Reinberg and Luis Dias Vales. Chromatin domains rich in inheritance. *Genes & Development*, 32(1):6–7, 2018.

[8] Ronald T Coleman and Gary Struhl. Causal role for inheritance of H3K27me3 in maintaining the OFF state of a Drosophila HOX gene. *Nature*, 546(6333):70–74, 2017.

[9] Christopher J Fryer, J Brandon White, and Katherine A Jones. Mastermind recruits CycC:CDK8 to phosphorylate the Notch ICD and coordinate activation with turnover. *Genes & Development*, 18(21):2269–2277, 2004.

[10] David Sprinzak, Abhinav Lakhanpal, Lauren LeBon, Leah A Santat, Mauricio E Fontes, Glenn A Anderson, William H Mather, and Michael B Elowitz. Cis-interactions between Notch and Delta proteins generate mutually exclusive signalling states. *Nature*, 465(7294):86–90, 2010.

[11] Haiqing Zheng, Bo Huang, Bingjie Zhang, Yinglin Xiang, Zhenhai Du, Qiaohong Xu, Yuanyuan Li, Qianqian Wang, Jing Ma, Xu Peng, et al. Quantitative dynamics of histone h3 methylation at the transcription start site area during ES cell differentiation. *Cell Research*, 24(7):890–893, 2014.

[12] Yupeng Zheng, Jeremiah D Tipton, Paul M Thomas, Neil L Kelleher, and Steve MM Sweet. Site-specific human histone H3 methylation stability: fast K4me3 turnover. *Proteomics*, 14(19):2190–2199, 2014.

[13] Ilya M Sobol. Global sensitivity indices for nonlinear mathematical models and their Monte Carlo estimates. *Mathematics and Computers in Simulation*, 55(1-3):271–280, 2001.

[14] Andrea Saltelli, Marco Ratto, Terry Andres, Francesca Campolongo, Jessica Cariboni, Debora Gatelli, Michaela Saisana, and Stefano Tarantola. Global sensitivity analysis: The primer. *John Wiley & Sons*, 2008.

[15] Andrea Saltelli. Making best use of model evaluations to compute sensitivity indices. *Computer Physics Communications*, 145(2):280–297, 2002.

[16] Andrea Saltelli, Paola Annoni, Ivano Azzini, Francesca Campolongo, Marco Ratto, and Stefano Tarantola. Variance based sensitivity analysis of model output. Design and estimator for the total sensitivity index. *Computer Physics Communications*, 181(2):259–270, 2010.

[17] Antoine Italiano, Jean-Charles Soria, Maud Toulmonde, Jean-Marie Michot, Carlo Lucchesi, Andrea Varga, Jean-Michel Coindre, Stuart J Blakemore, Adare Clawson, Bret Suttle, et al. Tazemetostat, an EZH2 inhibitor, in relapsed or refractory b-cell non-hodgkin lymphoma and advanced solid tumours: a first-in-human, open-label, phase 1 study. *The Lancet Oncology*, 19(5):649–659, 2018.

[18] Anthony W Tolcher, Wells A Messersmith, Slawomir M Mikulski, Kyriakos P Papadopoulos, Eunice L Kwak, Donald G Gibbon, Amita Patnaik, Gerald S Falchook, Arvind Dasari, Geoffrey I Shapiro, et al. Phase I study of ro4929097, a gamma secretase inhibitor of Notch signaling, in patients with refractory metastatic or locally advanced solid tumors. *Journal of Clinical Oncology*, 30(19):2348–2353, 2012.

[19] Quen J Cheng, Sho Ohta, Katherine M Sheu, Roberto Spreafico, Adewunmi Adelaja, Brooks Taylor, and Alexander Hoffmann. NF-κB dynamics determine the stimulus specificity of epigenomic reprogramming in macrophages. *Science*, 372(6548):1349–1353, 2021.

[20] Kevin L Morel, Alec V Sheahan, David L Burkhart, Sophia C Baca, Nadia Boufaied, Yang Liu, Xintao Qiu, Israel Cañadas, Katrin Roehle, Max Heckler, et al. EZH2 inhibition activates a dsrna-sting-interferon stress axis in cancer cells and sensitizes to immunotherapy. *Nature Cancer*, 2(4):444–456, 2021.

[21] Catrine Johansson, Anthony Tumber, Kaixiang Che, Peter Cain, Radoslaw Nowak, Carina Gileadi, and Udo Oppermann. The roles of Jumonji-type oxygenases in human disease. *Epigenomics*, 6(1):89–120, 2014.

[22] Milka Vinogradova, Victor S Gehling, Amy Gustafson, Shilpi Arora, Charles A Tindell, Catherine Wilson, Kaylyn E Williamson, Gulfem D Guler, Pranoti Gangurde, Wanda Manieri, et al. An inhibitor of kdm5 demethylases reduces survival of drug-tolerant cancer cells. *Nature Chemical Biology*, 12(7):531–538, 2016.